

Dung, N.T., Hay, R., Lesimple, A., Celik, K. and Unluer, C. (2021) Influence of CO<sub>2</sub> concentration on the performance of MgO cement mixes. *Cement and Concrete Composites*, 115, 103826.

(doi: [10.1016/j.cemconcomp.2020.103826](https://doi.org/10.1016/j.cemconcomp.2020.103826))

This is the Author Accepted Manuscript.

There may be differences between this version and the published version. You are advised to consult the publisher's version if you wish to cite from it.

<https://eprints.gla.ac.uk/234078/>

Deposited on: 17 February 2021

# Influence of CO<sub>2</sub> concentration on the performance of MgO cement mixes

N.T. Dung<sup>a</sup>, R. Hay<sup>b</sup>, A. Lesimple<sup>b</sup>, K. Celik<sup>b</sup>, C. Unluer<sup>c,\*</sup>

<sup>a</sup> School of Civil and Environmental Engineering, Nanyang Technological University,  
50 Nanyang Avenue, Singapore 639798, Singapore

<sup>b</sup> Civil Engineering, New York University in Abu Dhabi, Abu Dhabi, United Arab Emirates

<sup>c</sup> School of Engineering, University of Glasgow, G12 8LT, Glasgow, United Kingdom

\* Corresponding author. E-mail address: Cise.Unluer@glasgow.ac.uk

## Abstract

This paper investigated the influence of different CO<sub>2</sub> concentrations on the microstructural and mechanical development of reactive MgO cement (RMC) concrete. Combination of various analyses revealed the enhancement of hydrated magnesium carbonate (HMC) phases with relatively superior micro-mechanical properties as the CO<sub>2</sub> concentration increased from ambient (~0.04%) to accelerated (5-20%) levels. The higher CO<sub>2</sub> diffusion within samples cured under 5-20% CO<sub>2</sub> increased the compressive strength by ~5 times. While samples cured under 20% CO<sub>2</sub> revealed high early strengths, the formation of a dense HMC layer on the sample exterior led to limitations on further CO<sub>2</sub> diffusion. Use of 5% CO<sub>2</sub> produced comparable strengths as 20% CO<sub>2</sub> at 28 days, highlighting the potential of using lower concentrations. Samples cured under 10% CO<sub>2</sub> revealed the best performance at 28 days, thereby defining this environment as the most favorable condition for the development of microstructural and mechanical properties of RMC concrete.

**Keywords:** MgO cement; carbonation; CO<sub>2</sub> concentration; strength; microstructure

## 1 Introduction

Reactive magnesium oxide (MgO) cement (RMC) can potentially represent a sustainable alternative to ordinary Portland cement (OPC) due to its ability to absorb CO<sub>2</sub> while curing and potential to be recycled within a closed loop [1-4]. RMC is produced at significantly lower calcination temperatures than OPC (i.e. 700-900°C vs. 1450°C) [5]. Despite the higher CO<sub>2</sub> emissions associated with its production (i.e. 1.1 vs. 0.9 tonne/tonne of cement) [4], RMC can re-absorb some of the CO<sub>2</sub> emitted during its production, reducing its total CO<sub>2</sub> emissions and resulting in potentially more sustainable formulations, depending on the source of CO<sub>2</sub> [6, 7]. Furthermore, the production of RMC from magnesium silicates such as forsterite (Mg<sub>2</sub>SiO<sub>4</sub>) and serpentine (Mg<sub>3</sub>Si<sub>2</sub>O<sub>5</sub>(OH)<sub>4</sub>) can present a route without any CO<sub>2</sub> emissions [4, 8, 9]; while another attractive route for the extraction of RMC involves the use of reject brine obtained from desalination plants [10, 11].

The carbonation of Mg-phases is the primary process for strength development in RMC concrete. Carbonation is preceded by hydration, during which the dissolution of MgO is associated with an increase in the pH of the pore solution [12, 13], which promotes the absorption and dissolution of CO<sub>2</sub> for the subsequent carbonation process [14, 15]. The dissolved CO<sub>2</sub> reacts with Mg(OH)<sub>2(aq,s)</sub> to form hydrated magnesium carbonates (HMCs) during carbonation [16-18]. The formation of HMCs is associated with their expansive formation that reduces porosity and establishes an interconnected network to provide binding ability, thereby enabling strength gain within RMC samples [19-21]. The most common HMCs in carbonated RMC concrete are acicular artinite (Mg<sub>2</sub>CO<sub>3</sub>(OH)<sub>2</sub>·3H<sub>2</sub>O), rosette-like hydromagnesite (Mg<sub>5</sub>(CO<sub>3</sub>)<sub>4</sub>·(OH)<sub>2</sub>·4H<sub>2</sub>O) and needle-like nesquehonite (MgCO<sub>3</sub>·3H<sub>2</sub>O) [22-25]. The performance of RMC concrete is determined by the composition, morphology, and content of HMCs, which depend on the hydration and carbonation processes [26, 27].

Several studies [20, 26, 28] have looked into improving the strength development and density of RMC samples by accelerating the hydration and carbonation reactions. Accordingly, the use of 0.1 M magnesium acetate as a hydration agent increased the 3-day hydration degree of MgO by a factor of 1.5 (49% vs. 75%), resulting in an increase in the compressive strength by a factor of 2.5 [26]. Alternatively, curing the samples under the accelerated carbonation (5-20% CO<sub>2</sub>) stimulated the formation of HMCs and enabled a rapid strength gain within RMC samples [19, 26]. When compared with those cured under ambient conditions, RMC samples cured

under at 10% CO<sub>2</sub> revealed 28-day compressive strengths that were higher by a factor of 7 (4 vs. 28 MPa) [26]. The combined use of magnesium acetate under accelerated carbonation conditions led to an increase in the 28-day strength by a factor of 14 when compared with the control RMC sample cured under ambient conditions (4 vs. 56 MPa) [26]. This increase in compressive strength was attributed to the increase in the content and improvements in the morphology of HMCs, which were facilitated by the enhancement in the hydration and carbonation processes [29, 30].

In addition to the use of accelerated carbonation conditions, the introduction of 0.5-1% hydromagnesite as a nucleation seed stimulated the formation of HMCs within RMC concrete and increased the 28-day compressive strength by 33% (48 vs. 64 MPa) [20]. Furthermore, the simultaneous inclusion of magnesium acetate and nucleation seeds increased the 28-day compressive strength by 46% (48 vs. 70 MPa) when compared with the control sample [20]. The extensive formation of HMCs, which provided a continuous binding network, improved the sample microstructure by filling the pore space and establishing a dense microstructure, which translated into higher strengths and lower water absorption within carbonated RMC concrete samples [26]. The strength development of these samples was rapid at early ages (i.e. < 7 days) under accelerated carbonation conditions, continued by a slower increase at longer durations [6, 20].

Although previous studies [1, 19, 26] have demonstrated the influence of accelerated carbonation on the strength development of RMC samples, the influence of CO<sub>2</sub> concentration on the microstructural and mechanical properties of RMC concrete has not been fully revealed. While a few studies [19, 31] used CO<sub>2</sub> concentrations varying from 5% to 20%, the low hydration degree of MgO and the short curing periods investigated did not enable the identification of the influence of CO<sub>2</sub> concentration on the carbonation of RMC concrete samples. This is particularly important as the formation of HMCs initiates from the sample exterior towards the core, in line with the diffusion path of CO<sub>2</sub> [22], which depends on the CO<sub>2</sub> concentration. Therefore, understanding the role CO<sub>2</sub> concentration plays on carbonation depth and the implications of the carbonation reaction on the pore structure and profile of reaction products at different depths is essential. In this respect, the formation and properties of various HMCs within RMC concrete, as well as the microstructural and mechanical development of these samples under different CO<sub>2</sub> concentration have not been fully investigated. Therefore, further research is needed to improve the curing process for the

effective microstructural and mechanical development of RMC concrete, thereby enabling the efficient use of RMC.

With the goal of filling this gap, this paper presented a detailed study on RMC concrete subjected to different curing conditions. New insights on the formation of HMCs under different CO<sub>2</sub> concentrations were provided to reveal the microstructural and micromechanical properties of RMC samples. Concrete samples using magnesium acetate as a hydration agent were prepared and subjected to ambient (i.e. 0.04% CO<sub>2</sub>) and accelerated (i.e. 5, 10 and 20% CO<sub>2</sub>) carbonation conditions. Phase quantification was accomplished by XRD and TG-DTG analyses. The morphology of HMCs was observed via SEM. X-ray micro computed tomography (CT) was also applied to quantitatively analyze the influence of CO<sub>2</sub> concentration on the microstructural development of RMC samples in 3D. MIP and x-ray micro CT were utilized to evaluate the influence of different CO<sub>2</sub> concentrations on the pore structure and carbonation depth of samples, which was also evaluated by phenolphthalein indicator. FTIR and confocal Raman microscopy were used to identify the phase transformations under different CO<sub>2</sub> concentrations. Furthermore, nanoindentation was used to measure the elastic modulus of the carbonated RMC samples subjected to various CO<sub>2</sub> concentrations.

## **2 Materials and Methodology**

### **2.1 Materials**

RMC, produced at around 1000°C and supplied by Richard Baker Harrison (UK) was used in this study. The chemical composition and physical properties of RMC are shown in Table 1. Magnesium acetate ((CH<sub>3</sub>COO)<sub>2</sub>Mg), provided by VWR (Singapore), was used as a hydration agent at a concentration of 0.1 M (i.e. based on the findings of previous research [26]) to promote the hydration process. Aggregates used in the preparation of concrete samples were gravel in saturated surface dry condition with a particle size of 4.7–9.5 mm. The contaminants within the coarse aggregates were removed by properly cleaning them in a water tank prior to mixing.

## 2.2 Sample preparation and methodology

Magnesium acetate was dissolved in water prior to mixing with the dry components. The prepared concrete mixtures involved a magnesium acetate solution to binder ratio of 0.65; whereas the magnesium acetate solution to coarse aggregate ratio was 0.34. The corresponding paste samples (i.e. with the same solution to binder ratio) were cast into cylindrical moulds (5 mm in diameter and 13 mm in height). Cubic samples with dimensions of 20×20×20 mm were also prepared to study the influence of CO<sub>2</sub> concentration via mercury intrusion porosimetry (MIP).

In the preparation of concrete samples, fine aggregates were omitted to enable the extraction of the carbonated paste from the rest of the sample without any contamination and to increase the accuracy of phase quantifications. After mixing, 50×50×50 mm cubic concrete samples were cast, consolidated by a vibration table and levelled by a trowel. The cast samples were demoulded after 24 hours of casting and continuously cured under ambient (Amb) conditions (~0.04% CO<sub>2</sub>, ~80% relative humidity (RH) and ~30°C) or accelerated carbonation conditions in an environmental chamber (~80% RH and ~30°C), in which the CO<sub>2</sub> concentration changed from 5% to 10% and 20% for samples C5, C10 and C20, respectively. All samples were cured under respective environments for 28 days, until further testing. The corresponding cubic paste samples were also placed under the same conditions for the analysis of their internal structure. The cylindrical paste samples were covered on all sides except for the top to ensure that carbonation took place in one direction only.

The paste samples and segments, which had a diameter of 5-10 mm and a thickness of 1-2 mm, were extracted from the cubic concrete samples and stored in isopropanol for 7 days to stop hydration, and dried in vacuum prior to phase and microstructural analyses. These segments were further broken down to evaluate the presence of the pulverized coarse aggregates prior to grinding. The pulverized coarse aggregates were easily identified in these thin segments by the contrast in their colour (dark) with the colour of the MgO paste (white). Accordingly, the pulverized coarse aggregates were removed from the segments prior to further analysis. In preparation for FTIR, XRD and TG-DTG analyses, these segments were ground down to pass through a 75 µm sieve.

While all samples were prepared at the same time and under the same conditions, the compressive strength, XRD and TG-DTG results of sample C20 were obtained from previous work [22] to enable its direct comparison with the other samples presented in this study.

### **2.2.1 Compressive strength**

The compressive strength of the RMC concrete samples was measured in triplicates at 1, 3, 7, 14 and 28 days, at a loading rate of 55 kN/min, by a Toni Technik Baustoffprüfsysteme machine.

### **2.2.2 Phase identification and quantification**

The FTIR spectra of the samples were recorded using a FTIR spectrometer (Cary 670, Agilent) fitted with a diamond attenuated total reflectance (ATR) accessory. The powder samples were deposited directly on to the diamond lens of the spectrometer. The spectra were collected in transmission mode at a resolution of  $1\text{ cm}^{-1}$ . For each sample, 32 scans were recorded and averaged out in the range of  $800\text{-}1900\text{ cm}^{-1}$ , where the main vibration bands of HMCs were observed.

Confocal Raman spectra were recorded for samples at 7 days using a confocal Raman microscope by Alpha300 RA from WITec GmbH (Ulm, Germany). Before testing, calibration was performed on a silicon wafer to ensure the alignment of the instrument. A scan over an area of  $170\times 170\text{ }\mu\text{m}$  was conducted under a resolution of 170 points/line and a line spacing of  $1\text{ }\mu\text{m}$ . A high-resolution scan over Raman shifts of  $50\text{ cm}^{-1}$  and  $1250\text{ cm}^{-1}$  was achieved by tuning the detector to a graze of 1800 grooves per millimeter. The obtained spectrum data were analyzed with Project 5.0 software from Witec. In addition to the average spectrum, component analysis was also performed to identify the distribution of carbonation products on the sample surfaces.

The hydrate and carbonate phases were quantified via XRD and TG-DTG analyses. XRD patterns were recorded on a Philips PW 1800 spectrometer using  $\text{Cu K}\alpha$  radiation (40 kV, 30

mA), at a step size of  $0.017^{\circ} 2\theta$ , and a  $2\theta$  range of  $5-70^{\circ}$ . Rietveld analysis was performed on the XRD data by using the X'Pert HighScore Plus software for quantification purposes.

TG-DTG was performed on a Perkin Elmer TGA 4000 instrument, operated at a heating rate of  $10^{\circ}\text{C}/\text{min}$  between  $30^{\circ}\text{C}$  and  $950^{\circ}\text{C}$ , under nitrogen flow. To quantify the amount of hydrate and carbonate phases, the areas corresponding to each decomposition step in DTG curves were deconvoluted.

### **2.2.3 Microstructural analysis**

The vacuum dried samples were coated with gold before SEM analysis to observe the morphology of the carbonate phases within samples by using a Zeiss Evo 50 microscope.

An X5000 CT scanner from North Star Imaging Inc. was used to obtain radiographs of samples. Molding clay and perforated foam were used to fix the sample onto the stage, whose distance from the x-ray source was set at approximately 90 mm. Scans were acquired at a working voltage of 120 kV and current of 300  $\mu\text{A}$ . A delay time of 100 milliseconds was adopted and a total of 2500 projections with an average of 9 frames/projection were collected for 3D construction. This setup led to a resolution of approximately 10  $\mu\text{m}$ . A geometry with a spacing of 0.762 mm was used for data calibration. The rendering and extraction of 2D slices were performed with proprietary software by X View CT (eFX-view), while the reconstruction of 3D images and their analysis were done with Avizo 9.5, a visualization and computation software used for 3D data sets.

The average porosity and pore size distribution of cubic paste samples were determined using AutoPore IV 9500 high-pressure MIP system (Micromeritics') with a pressure capacity of up to 60,000 psi. The obtained MIP data was refined using locally weighted scatterplot smoothing (Lowess) to evaluate the average pore size distribution of each sample.

### **2.2.4 Carbonation depth**



The influence of different CO<sub>2</sub> concentrations on 1- and 3-dimensional carbonation diffusion was studied on cylindrical paste and cubic concrete samples, respectively. The carbonation of cylindrical paste samples took place in only 1 direction as the sides of the samples were covered by the mould. The carbonation depth of the paste samples was measured via x-ray micro CT images, during which the results were recorded by taking the average depth of 5 samples.

On the other hand, the depth of 3D carbonation observed within concrete samples was analyzed by measuring the depth of the colourless region using phenolphthalein indicator. To initiate the analysis, the cubic concrete samples were split and the freshly split surfaces were cleaned and sprayed with a 1% phenolphthalein solution [32]. The recorded results were the average of carbonation depths taken from 24 locations on 3 different samples.

### **2.2.5 Nano-indentation**

Samples ranging in size from 5 mm to 10 mm were embedded in epoxy and polished sequentially to 0.05  $\mu\text{m}$  with oil suspended diamond particles. The exposed surfaces were subjected to nanoindentation, which was performed with Keysight G-200 Nanoindenter under a diamond Berkovich tip. The loading was initiated when a stiffness of 200 N/m was detected on the surface. A target indentation depth of 350 nm was used to achieve an optimum interaction volume larger than the nanogranular globules [33] but smaller than the homogeneous isotropic region of a typical phase [34]. At this depth, the corresponding load was held for 10 s to minimize the effects of creep and thermal drift. As both the elastic and plastic deformation occur during loading in a typical indentation experiment, the early portion of the unloading curve was used to quantify the elastic modulus ( $E_p$ ), which was estimated from Equation 1, where  $E_r$  is the resultant or effective indentation modulus,  $\nu$  is the Poisson's ratio of the test material, and  $E_i$  and  $\nu_i$  are the elastic modulus and Poisson's ratio of the indenter (for a diamond tip,  $E_i = 1141$  GPa and  $\nu_i = 0.07$  [35]), respectively. Poisson's ratios of 0.18-0.27, 0.20 and 0.25 were reported for MgO [36], Mg(OH)<sub>2</sub> (MP-30247) and MgCO<sub>3</sub> (MP-5348) [37], respectively. Considering the multi-phase hydration and carbonation products observed in carbonated RMC samples, a Poisson's ratio of 0.24 [22] was applied in the stiffness calculation. It must be noted that the second power relationship shown in Equation 1 implies that a Poisson's ratio ranging between 0.18-0.27 would have a small effect on the material indentation modulus. An 8×8 grid at a spacing of 50  $\mu\text{m}$  was performed on each sample.

$$1/E_r = (1-\nu^2)/E_p + (1-\nu_i^2)/E_i \quad (1)$$

### 3 Results

#### 3.1 Compressive strength

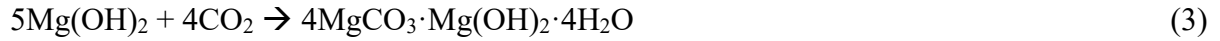
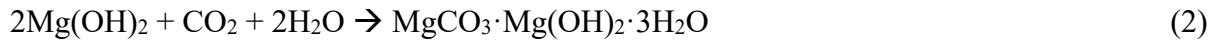
The compressive strength of RMC concrete samples under different CO<sub>2</sub> concentrations is presented in Fig. 1. In line with the findings of previous studies [19, 26, 38], the use of elevated carbonation concentrations (5-20%) produced significantly higher compressive strengths than the ambient condition. While the compressive strength of samples cured under accelerated carbonation continuously increased with time, those kept under ambient conditions demonstrated a very slow strength development during the first few days, which reached a plateau after 7 days. As a majority of the strength gain was initially dependent on the hydration process at early stages, the 1-day compressive strengths of Amb, C5, C10 and C20 samples were relatively comparable. When compared to the 1-day values, the compressive strengths of carbonated samples increased by up to 8 times during the first 14 days, reaching 48-58 MPa at 14 days. In contrast, Amb sample revealed a strength of only 11 MPa after 14 days of curing. These results indicated the importance of subjecting RMC concrete samples to accelerated carbonation conditions for a rapid strength gain.

While the effect of different CO<sub>2</sub> concentrations on the performance of concrete samples was not obvious initially, strength development was directly correlated with CO<sub>2</sub> concentration from 3 days until 14 days of curing. The use of 10% CO<sub>2</sub> concentration, as commonly applied in previous studies [26, 27] produced lower compressive strengths than those obtained under 20% CO<sub>2</sub> at 7 and 14 days, after which the difference between these two sets diminished over time, leading to the highest 28-day strength (63 MPa) achieved by samples cured under 10% CO<sub>2</sub>. On the other hand, at earlier stages (i.e. 7 days), the compressive strength of C20 sample was 23% (51 vs. 44 MPa) and 50% (51 vs. 34 MPa) higher than that of C10 and C5 samples, respectively. Accordingly, when compared with curing under 5% and 10% CO<sub>2</sub>, subjecting the samples to 20% CO<sub>2</sub> could shorten the curing period by 50% as the 7-day compressive strength of C20 sample was similar to those of C5 and C10 samples at 14 days, respectively. The early high strengths of samples cured under 20% CO<sub>2</sub> could be attributed to the increased diffusion

of CO<sub>2</sub> and thereby the higher carbonation degree within these samples. Although using a lower CO<sub>2</sub> concentration of 5% revealed lower strengths initially, these samples caught up with the rest and presented similar 28-day strengths as those cured under 20% CO<sub>2</sub> (58-60 MPa). These results highlighted that in circumstances where samples can be left to cure for longer durations, using lower CO<sub>2</sub> concentrations (e.g. 5%) can also enable RMC samples to eventually demonstrate their strength gain potential.

### 3.2 FTIR

The FTIR spectra of the RMC-based concrete samples cured under varying CO<sub>2</sub> concentrations for 7 and 28 days are shown in Fig. 2 (a) and (b), respectively. The broad peak at ~1420 cm<sup>-1</sup> observed in Amb sample, assigned to CO<sub>3</sub><sup>2-</sup> [39], indicated the small quantity of carbonates forming under ambient conditions, which did not change with curing duration. This stability in the presence of carbonate phases could explain the lack of improvement in the compressive strength of Amb sample, which remained significantly low ( $\leq 12$  MPa) regardless of the curing duration. However, as the CO<sub>2</sub> concentration increased to 5% in C5 sample, the band referring to CO<sub>3</sub><sup>2-</sup> became sharper with multiple centers located at ~1423 cm<sup>-1</sup> and ~1484 cm<sup>-1</sup>, corresponding to the antisymmetric stretching vibration of CO<sub>3</sub><sup>2-</sup> in the HMC phases [23, 25]. The intensity of this band in C5 sample at 28 days was nearly doubled when compared to the one observed at 7 days, representing the enhancement in the formation of carbonates. A similar trend was observed for C10 sample cured under 10% CO<sub>2</sub>, where the bands referring to the presence of carbonate phases became more prominent as the curing duration increased, in line with the increase in the strength of these samples. The shoulder observed at ~1517 cm<sup>-1</sup> in C10 sample at 28 days was exclusive to the antisymmetric stretching vibration of CO<sub>3</sub><sup>2-</sup> within nesquehonite [23, 25, 40]. As the CO<sub>2</sub> concentration increased to 20% in C20 sample, the 1517 cm<sup>-1</sup> peak became more pronounced, which was especially clear at 28 days. When compared with other HMCs, the higher solubility product constant of nesquehonite ( $10 \times 10^{-5.7}$  vs.  $10 \times 10^{-38.3}$  of hydromagnesite and  $10 \times 10^{-19}$  of dypingite [6, 41-43]), as well as the higher CO<sub>2</sub>/Mg(OH)<sub>2</sub> molar ratio required for its formation (Equations 2-4), could explain the increased formation of nesquehonite under high CO<sub>2</sub> concentrations used during the curing of C20 sample. The effect of curing duration (i.e. 7 vs. 28 days) on the increased formation of this phase in C20 sample was in agreement with the strength results (51 vs. 60 MPa).



### 3.3 Confocal Raman microscopy

Fig. 3 presents the Raman spectra obtained from the external surfaces of RMC samples cured under varying  $\text{CO}_2$  concentrations for 7 days. Raman spectra obtained from RRUFF database were consolidated for brucite (R040077), nesquehonite (R050639), hydromagnesite (R060011), dypingite (R070086) and artinite (R060166). The database revealed that the peaks at  $\sim 277 \text{ cm}^{-1}$ ,  $444 \text{ cm}^{-1}$ ,  $726 \text{ cm}^{-1}$  and  $1084 \text{ cm}^{-1}$  were due to  $\text{OH}^-$  vibration in  $\text{Mg}(\text{OH})_2$ . The peaks associated with  $\text{CO}_3^{2-}$  vibration in carbonation products were in the vicinity of  $\sim 1100 \text{ cm}^{-1}$ , which was slightly shifted to the right when compared with the prominent vibration peak of  $\text{OH}^-$  in brucite ( $1084 \text{ cm}^{-1}$ ). These Raman spectra obtained from the database were consistent with the expected appearance of nesquehonite at  $1098 \text{ cm}^{-1}$  [44], hydromagnesite at  $1121 \text{ cm}^{-1}$  [45] and artinite at  $1092 \text{ cm}^{-1}$  [46]. Due to the overlap between the spectra of artinite and nesquehonite, the “artinite/nesquehonite” convention was used to refer to these phases throughout the text. The Amb sample showed peaks at  $279 \text{ cm}^{-1}$ ,  $444 \text{ cm}^{-1}$  and  $1084 \text{ cm}^{-1}$ , which were associated with  $\text{OH}^-$  vibration in brucite, resulting from the hydration of RMC. The presence of both artinite/nesquehonite and hydromagnesite were apparent in C5 sample at  $1097 \text{ cm}^{-1}$  and  $1119 \text{ cm}^{-1}$ , respectively. The coexistence of these carbonate phases under 5%  $\text{CO}_2$  changed into the domination of hydromagnesite on the sample surfaces as the  $\text{CO}_2$  concentration increased to 10% and 20%. Notably, the spectrum corresponding to  $\text{OH}^-$  vibration in brucite disappeared in both C10 and C20 samples as a result of the complete carbonation in exterior regions when these samples were exposed to a minimum  $\text{CO}_2$  concentration of 10%  $\text{CO}_2$ .

The distribution of brucite, artinite/nesquehonite and hydromagnesite over the sample surfaces was also analyzed by applying a filter with a width of  $10 \text{ cm}^{-1}$  over the area scan spectrums at  $1086 \text{ cm}^{-1}$ ,  $1100 \text{ cm}^{-1}$  and  $1118 \text{ cm}^{-1}$ , respectively. The analysis was performed on C5 and C20 samples after 7 days of carbonation, whose results are depicted in Fig. 4. The accelerated

carbonation conditions these samples were subjected to resulted in small traces of brucite on the sample surfaces. As reflected by the normalized color intensity of brucite, increasing the CO<sub>2</sub> concentration did not significantly influence the carbonation of the exterior regions of the samples. A difference in phase distribution was also revealed through the mapping. While C5 sample showed the coexistence of artinite/nesquehonite and hydromagnesite, C20 sample demonstrated the domination of hydromagnesite.

### 3.4 XRD

Fig. 5 presents the XRD patterns of 7-day RMC concrete samples cured under different CO<sub>2</sub> concentrations. The internal standard, fluorite (CaF<sub>2</sub>), was observed at 28.2° 2θ. The main peaks of uncarbonated brucite (Mg(OH)<sub>2</sub>) and unhydrated periclase (MgO) were observed at 38.1° and 42.9° 2θ, respectively. Nesquehonite (MgCO<sub>3</sub>·3H<sub>2</sub>O), hydromagnesite (Mg<sub>5</sub>(CO<sub>3</sub>)<sub>4</sub>·(OH)<sub>2</sub>·4H<sub>2</sub>O) and artinite (Mg<sub>2</sub>CO<sub>3</sub>(OH)<sub>2</sub>·3H<sub>2</sub>O) were the main carbonation products observed in the XRD patterns. The main peaks of artinite, hydromagnesite and nesquehonite were observed at 13.7°, 15.2° and 32.8° 2θ, respectively. A comparison of the uncarbonated brucite content with respect to the intensity of the internal standard revealed lower intensities of brucite within the samples kept under accelerated carbonation conditions than those observed in Amb sample.

The influence of CO<sub>2</sub> concentration on the composition of RMC concrete samples carbonated for 7 days is shown in Table 2. In line with the FTIR results, the use of accelerated carbonation enhanced the conversion of brucite to various HMC phases. Artinite and nesquehonite were the main carbonate phases observed within the samples kept under accelerated carbonation for 7 days. An increase in the CO<sub>2</sub> concentration to 20% stimulated the formation of all HMCs (i.e. artinite, hydromagnesite and nesquehonite), resulting in the highest HMCs content in C20 sample, which could explain the corresponding increase in the strength of these samples. However, the use of higher CO<sub>2</sub> concentrations also resulted in a lower conversion of MgO to brucite, evident by the higher periclase contents of C10 and C20 samples (27.4% and 34.9%) in comparison to C5 and Amb samples (19.7% and 16.8%). This could be partially attributed to the increased formation of HMCs within C10 and C20 samples under high CO<sub>2</sub> concentrations, thereby covering the surfaces of unhydrated MgO grains and preventing their further contact with water for further hydration.

### 3.5 TGA

The TG-DTG results of RMC concrete samples cured under different CO<sub>2</sub> concentrations for 7 and 28 days are shown in Fig. 6 and 7, respectively. C5, C10 and C20 samples showed significantly higher total mass loss values than Amb sample, which was attributed to the higher decomposition, and hence the higher contents of HMCs within the carbonated samples. This increase in the mass loss of these samples confirmed the role of CO<sub>2</sub> concentration in providing higher carbonation degrees and thereby improved strengths when compared to Amb sample, which was cured under ambient conditions for the same duration. The endothermic peak at ~100°C corresponded to the dehydration of water bonded to HMCs [8, 47]. The strong endothermic peak at ~350-380°C was responsible for the decomposition of uncarbonated brucite, the dehydroxylation (e.g. artinite and hydromagnesite) and decarbonation (e.g. nesquehonite) of HMCs [8, 47]. Additionally, endothermic peaks at ~520°C and 600°C were associated with the decarbonation of HMCs [48-50].

The mass loss corresponding to the dehydration, dehydroxylation and decarbonation steps, obtained by calculating the area of the deconvoluted DTG curves, along with the total mass loss of each sample, are presented in Table 3. The majority of the mass loss observed in each sample corresponded to the dehydroxylation of brucite and HMCs. After 7 days of curing, the mass loss corresponding to decarbonation within samples subjected to accelerated carbonation were 52-85% higher than that of Amb sample (3.3% vs. 5.0-6.1%). The use of increased CO<sub>2</sub> concentrations in C5, C10 and C20 samples also led to an increase in the mass loss due to dehydration by 3.3-4.6 times when compared to Amb sample (2 vs. 6.5-9.1%). Increasing the curing duration from 7 to 28 days also led to an increase in the mass loss at all stages, thereby translating into higher mass losses within all samples at 28 days. This increase in the mass loss values indicated the continuation of the hydration and carbonation reactions over time. Despite their lower carbonation rate at 7 days, C10 sample subjected to 10% CO<sub>2</sub> revealed a higher carbonation degree than C20 sample cured under 20% CO<sub>2</sub> at 28 days, which was reflected by its slightly higher mass loss due to decarbonation (6.8% vs. 6.6%). Furthermore, sample C10 demonstrated a higher mass loss associated with dehydroxylation than sample C20 (24.2% vs. 22.7%). This increase in the mass loss of C10 sample after 28 days can explain its higher corresponding compressive strength than C20 sample (63 vs. 60 MPa). Alternatively, despite

its highest total mass loss, C5 sample revealed a lower mass loss due to decarbonation (6.2%) than C10 and C20 samples (6.8% and 6.6%), which could explain its slightly lower 28-day performance (58 MPa).

### 3.6 Microstructure

Fig. 8 reveals the microstructures of RMC samples subjected to different CO<sub>2</sub> concentrations for 7 days. When compared to the microstructure of Amb sample that was cured under ambient conditions (Fig. 8(a)), samples cured under accelerated carbonation conditions (Fig. 8(b)-(d)) revealed an extensive formation of various HMC phases with different morphologies. Needle-like artinite/nesquehonite and disk-like hydromagnesite were widely spread in C5, C10 and C20 samples. Alternatively, very few carbonate crystals with a diameter of ~0.1 μm were spotted among the generally uncarbonated paste of the Amb sample (Fig. 8(a)). Increasing the CO<sub>2</sub> concentration to 5% stimulated the formation of disk-like carbonates with a diameter of up to ~1 μm in C5 sample (Fig. 8(b)). Sample C10 cured under 10% CO<sub>2</sub> was composed of a mix of various carbonate crystals with different morphologies. Disk-like carbonates with a diameter of up to ~3 μm growing on the surface of needle-like carbonates with a diameter of ~1 μm was observed in C10 sample (Fig. 8(c)). When compared with C5 sample, C10 sample revealed the formation of bigger carbonate crystals, that were clustered into large agglomerates (i.e. ~6 vs. 10 μm in diameter). Moreover, these clusters were composed of crystals that seemed to bond well and form a connecting network in C10 sample, which differed from the segregated formation of carbonate particles observed in C5 sample. Increasing the CO<sub>2</sub> concentration to 20% in C20 sample (Fig. 8(d)) led to the widespread formation of thick carbonate needles (up to ~2 μm in diameter and >25 μm in length) that could be attributed to nesquehonite and artinite, whose surface were sparsely covered with clusters of disk-like hydromagnesite (up to ~3 μm in diameter). Differing from C5 and C10, C20 sample revealed a dense layer of needle-like carbonate crystals that merged into each other, thereby forming an impermeable structure, which could have contributed to the improved performance of C20 sample at 7 days.

### 3.7 Pore structure

Vertical cross sections obtained from x-ray micro CT reconstruction of RMC paste samples cured under different CO<sub>2</sub> concentrations are shown in Fig. 9. The appearance of air bubbles could be associated with the lack of proper consolidation during the casting of the paste, which was relatively challenging due to the small mould size used. The variation in the greyscale intensity along the sections was attributed to the change in mass density as a result of carbonation. Accordingly, the brightest tone observed at the top of the samples corresponded to the dense structure of HMCs. The higher mass density of HMCs resulted in increased X-ray attenuation and a lighter greyscale under tomographic reconstruction. Furthermore, the lighter grey tone observed in regions along the sample surface was attributed to the presence of HMCs, which was enabled by the diffusion of CO<sub>2</sub> and moisture through the sides of the sample via the formation of a gap between the sample and the wall of the plastic mould. The transverse cracks observed in carbonated samples could be attributed to the tensile stress induced by the expansion of HMCs throughout different regions that were restrained by uncarbonated sections. This difference in phase formations resulted in phase incompatibility, thereby causing a restraint upon re-exposure to ambient environment and subsequent drying.

Computations were made on Avizo to comparatively evaluate the porosity of the samples within the top and middle regions of interest (ROIs). Due to the limitation on the voxel resolution achievable with the equipment, only pores in the size range of 10-100  $\mu\text{m}$  ( $4.2 \times 10^3$ - $4.2 \times 10^6 \mu\text{m}^3$  equivalent spherical volume) corresponding to entrapped air voids [51] were analyzed. Also, to eliminate the effect of carbonation within the wall region, the ROIs were limited to the interior  $2 \times 2 \times 1.5$  mm volume. The greyscale of all images was first partitioned and Porosities Wizard module of the Avizo software was implemented with thresholds consistently assigned to voids and materials. Results of the cumulative pore volume relative to sample volume versus pore size (expressed in equivalent volume) are presented in Fig. 10 for C10 and C20 samples. The top regions of both C10 and C20 samples exhibited lower porosities when compared to their corresponding middle regions due to the higher carbonation degrees observed in the former. The top region of C10 sample revealed a higher porosity than that of C20 sample, which was consistent with the increased formation of HMCs in C20 sample, as reported earlier in Sections 3.4 and 3.5. The dense exterior of C20 sample played a dominant role in the superior mechanical performance of this sample at 7 days. A reduction in the porosity of C10 sample when compared to C20 sample was observed in the middle region, which could be due to the enhanced carbonation of the former. The more porous outer section of C10 may have facilitated the continuous diffusion of CO<sub>2</sub> throughout the sample, thereby



slightly enhancing the carbonation of the interior region. 3D visualization of the pores in C10 and C20 samples shown in Fig. 11 revealed the presence of cracks within the top regions as depicted by extended void volumes, which were not included in the calculation of the cumulative void volume.

The MIP results revealed the average porosity and pore size distribution of RMC paste samples cured under different CO<sub>2</sub> concentrations for 7 days, as shown in Fig. 12. Amb sample cured under ambient conditions led to the highest average porosity (37%), with a pore size distribution peak centred at ~0.3 µm. Although the use of accelerated carbonation curing at a CO<sub>2</sub> concentration of 5% did not have a significant influence over the pore size distribution, the average porosity of C5 sample dropped by nearly 15% when compared with the Amb sample. This reduction in porosity was attributed to the densification of C5 sample due to the formation of HMCs, as reported earlier. When the samples were subjected to 10% CO<sub>2</sub>, the average porosity dropped marginally, while a remarkable change was observed in the pore size distribution, which became bimodal due to the emergence of a broad distribution peak centred at ~0.02 µm. This reflected a major microstructural change accompanied with an accelerated formation of carbonation products over the sample volume, leading to a significant drop in the average pore size. Similarly, when the samples were subjected to 20% CO<sub>2</sub>, a marginal shift in the broad distribution peak to ~0.01 µm was observed. The remaining peak centred at 0.3 µm with a higher intensity in C20 sample revealed the inhibition of further CO<sub>2</sub> diffusion towards the inner sample, leading to the formation of HMCs on the sample surfaces. Curing under 20% CO<sub>2</sub> resulted in the lowest porosity in C20 sample (18%), consistent with the significant formation of dense HMC phases such as artinite, nesquehonite and hydromagnesite, as observed in XRD and SEM analyses. The lower overall porosity as well as the shift in the pore size distribution revealed by C20 sample relate well with the compressive strength results. Accordingly, an increase in strength from 11 MPa to 51 MPa was observed with an increase in the CO<sub>2</sub> concentration from ~0.04% to 20% after 7 days of curing, confirming the direct relationship between the densification of the pore structure and mechanical performance.

### **3.8 Carbonation depth**

The one dimensional carbonation depth of the carbonated samples at 7 days was measured at five locations spaced at 1 mm intervals, starting at ~0.5 mm from the sample surface. The

average carbonation depth results, along with the corresponding standard deviation values, are presented in Fig. 13. The carbonation depths of C5, C10 and C20 samples at 7 days were recorded as 0.7 mm, 1.9 mm and 1.2 mm, respectively.

The 3 dimensional carbonation diffusion of concrete samples was also monitored via the change in pH of their pore solution. Phenolphthalein, which turns colorless when the pH of the pore solution is below 9 [52], was used as the pH indicator to assess the carbonation depth. Accordingly, Fig. 14 presents the progress of the carbonation depth in RMC samples during 28 days of curing, as measured by the depth of the colorless region. It should be noted that the measurement of carbonation depth in RMC samples would be more sensitive than that of PC samples due to the lower pH of the pore solution of the former ( $\sim 10.5$  vs.  $\sim 12.5$  [6, 52]). The obtained results clearly indicated the influence of  $\text{CO}_2$  concentration on the carbonation depth during the initial stages of curing. Consequently, higher  $\text{CO}_2$  concentrations stimulated the diffusion of  $\text{CO}_2$  and resulted in the highest carbonation depth in C20 sample on the first day (11 mm vs. 0.5-8.8 mm). This higher carbonation depth translated into the densification of the exterior layers, which partially inhibited the further diffusion of  $\text{CO}_2$  at greater depths within C20 sample. Therefore, C20 sample revealed a lower carbonation depth than C10 sample after 3 days (18 mm vs. 17 mm). While the carbonation depth of C20 sample plateaued after 7 days at 18 mm, that of C10 sample reached 21 mm after 28 days of carbonation. This trend was in line with the strength results (Fig. 1), where C10 sample surpassed others at 28 days. Although C5 sample revealed a fast development in terms of its carbonation depth during the first 7 days of curing (from 3 mm to 16 mm), this was followed by a relatively stable level of carbonation afterwards. C5 sample demonstrated the lowest carbonation depth amongst all carbonated samples at 28 days (15.6 mm vs. 18-20.7 mm), which agreed with its relatively lower strength than those of C10 and C20 samples at 28 days. On the other hand, a consistent increase in the carbonation depth of Amb sample was observed, albeit low. The porous structure of this sample that was cured under ambient conditions enabled the continuous diffusion of  $\text{CO}_2$ , reaching 9 mm at 28 days.

### 3.9 Nano-indentation

Relative frequency plots for indentation modulus values of all the samples cured under different  $\text{CO}_2$  concentrations for 7 days are given in Fig. 15. In comparison to the ambient curing

condition, the 20% CO<sub>2</sub> environment greatly enhanced the micro-mechanical properties of the composite, as reflected by a notable reduction of low-modulus phase in C5, C10 and C20 samples (Fig. 15(b), (c) and (d)). The small existence of high modulus phases in the Amb sample could be attributed to the sporadic presence of artinite or accumulated hydromagnesite, as observed by SEM analysis. Contrary to the compressive strength results at 7 days, increasing the CO<sub>2</sub> concentration did not lead to a proportionate increase in the relative frequency of high modulus phases. C5 and C20 samples showed similar distributions of the indentation elastic modulus data. The average modulus for HMCs of C5 and C20 samples, estimated by implementing deconvolution with Gaussian fits, was in the range of 17.5-18.2 GPa; whereas the average modulus of HMCs in C10 sample increased to 22.3 GPa. The results confirmed that, in addition to an enhanced carbonation depth, as visually observed from x-ray micro CT images and pH indicator results, curing the samples under 10% CO<sub>2</sub> induced the formation of carbonate phases with relatively superior micro-mechanical properties.

Fig. 16 shows the relative frequency plots of indentation modulus results of C10 and C20 samples after 28 days of carbonation. Both samples exhibited an improvement in their relative frequency for high modulus phases at 28 days when compared to 7 days. This increase could be due to the formation of additional HMCs as carbonation proceeded over time, leading to the enhancement of the micro-mechanical property and the corresponding upward trend in the compressive strength results. While C20 sample was characterized by carbonation phases with an average indentation modulus of 17.5 GPa, a more dispersed distribution was observed for C10 sample at 28 days, with two major carbonation phases at 7.8 GPa and 22.3 GPa. The formation of the higher modulus phase, coupled with the progression of the carbonation front, contributed to the superior mechanical performance of C10 sample at 28 days.

#### **4 Discussion**

The formation of HMCs is associated with the provision of binding properties and volumetric expansion that enables the densification of microstructure, as demonstrated by SEM and x-ray micro CT images, thereby facilitating strength gain in RMC concrete. This study aimed to determine the optimum curing conditions for the formation of HMCs. Since the favorable RH for the formation of HMCs was determined as ~80% [31], the concentration of CO<sub>2</sub> was varied from 0.04% to 20% to determine its effect on the conversion of RMC to HMCs. Lower CO<sub>2</sub>

concentrations present in the ambient conditions led to a limited conversion of brucite into HMCs. The use of elevated CO<sub>2</sub> concentrations (5-20%) significantly accelerated the carbonation of brucite to increase the content of HMCs with improved morphologies, resulting in noticeable strength gain. Accordingly, the improved performance of RMC concrete samples under higher CO<sub>2</sub> concentrations was accompanied with the formation of HMC crystals with larger sizes for the first 7 days of curing. In line with the trend observed in compressive strength results, the TGA and carbonation depth measurements indicated a slower rate of HMC formation after 7 days of curing, which agreed with the findings of previous studies [41].

When the effect of different CO<sub>2</sub> concentrations on the progress of carbonation was investigated, an increase in the carbonation depth with an increase in the CO<sub>2</sub> concentration from 5% to 10% was observed, in line with the higher carbonation degree of the latter under higher concentrations of CO<sub>2</sub>. Alternatively, the reduction in carbonation depth observed in C20 sample cured under 20% CO<sub>2</sub> could be due to the accelerated formation of HMCs within the exterior regions of the sample, resulting in the densification of the microstructure and the inhibition of further CO<sub>2</sub> diffusion. Furthermore, the rapid formation of HMCs around unhydrated MgO grains prevented any further contact of these particles with water, thereby limiting the progress of hydration and carbonation within C20 sample. This was also revealed by the higher content of unhydrated MgO in C20 sample than in C10 sample. These findings could be an indication for the favorable condition provided via the combination of ~80% RH and 10% CO<sub>2</sub> for continuous CO<sub>2</sub> diffusion, thereby presenting an advantage for the increased formation of HMCs. This favourable condition was postulated to contribute to the further carbonation of the exterior regions and progression of the carbonation front, which ultimately led to improved mechanical performance at longer durations when compared to other samples subjected to lower or higher CO<sub>2</sub> concentrations. This finding was also supported by the higher 28-day strength of sample C10 than others (63 MPa vs. 60MPa), as shown in Fig. 1.

In addition to the improvement in the mechanical performance, the densification of sample microstructures associated with the formation of insoluble HMCs, as demonstrated by MIP results, could present an advantage in terms of long-term durability by inhibiting the ingress of aggressive chemicals in RMC concrete. While HMCs are known to be stable at pH values of > 7 [41, 53], the evaluation of their transformation into different forms under high temperatures also revealed their stability under varying conditions [41, 54]. Alternatively, the relatively limited formation of HMCs and the high residual periclase and brucite contents within all

samples (i.e. especially those of C10 and C20) were an indication of the potential of these samples to gain much higher strengths than those reported in Section 3.1 (Fig. 1) via the increased conversion of RMC into carbonate phases. This could be achieved via the integration of other practical methods to improve the hydration/carbonation of RMC and brucite. Accordingly, the introduction of synthesized HMCs into RMC blends, along with the use of a hydration agent, could further enhance the hydration of RMC [8, 55]; while the use of nucleation seeding or carbonation agents could further accelerate the conversion of brucite into HMCs [6, 29].

## 5 Conclusions

This study investigated the microstructural and micromechanical development of RMC concrete under different CO<sub>2</sub> concentrations. The content, morphology and distribution of various carbonate phases within the sample microstructure were evaluated. Use of ambient concentrations of CO<sub>2</sub> (0.04%) limited the formation of HMCs within RMC concrete samples and resulted in low compressive strengths (12 MPa at 28 days). Alternatively, elevated CO<sub>2</sub> concentrations ranging from 5% to 20% led to an improved CO<sub>2</sub> diffusion and accelerated the carbonation reaction. This enhancement of the reaction mechanism was accompanied with an increase in the content of HMCs with improved morphologies, which translated into higher compressive strengths (58-63 MPa at 28 days).

The effectiveness of accelerated carbonation was revealed by the performance of samples cured under 20% CO<sub>2</sub>, whose compressive strength at 7 days was equivalent to those of samples cured under 5% or 10% CO<sub>2</sub> at 14 days. In addition to the increased formation of HMCs, the establishment of a well-connected carbonate network enabled the samples cured under 20% CO<sub>2</sub> to outperform others at early ages. The dense carbonate layer that formed on the exterior sections of the samples influenced the rate of further CO<sub>2</sub> diffusion and consequently, the overall microstructural and mechanical performance. Despite their high strengths obtained at early ages, samples cured under 20% CO<sub>2</sub> demonstrated a slower strength development due to the dense surface layer that formed during the initial stages of carbonation, resulting in a porous inner structure and lower modulus of HMCs when compared with those cured under 10% CO<sub>2</sub>. Alternatively, the continuous diffusion of CO<sub>2</sub> in samples cured under 5% or 10% CO<sub>2</sub> enabled the higher utilization of RMC as a binder (i.e. smaller amounts of unreacted MgO remained in

the matrix), resulting in very similar 28-day strengths as those of samples cured under 20% CO<sub>2</sub> (58-63 MPa).

Combination of MIP, carbonation depth, x-ray micro CT and nano-indentation results revealed that curing RMC samples under 5-20% CO<sub>2</sub> induced the formation of carbonate phases with relatively superior micro-mechanical properties. However, the outcome of most analyses highlighted the comparable, if not superior, performance of samples cured under 10% CO<sub>2</sub> than others investigated in this study, thereby defining this environment as the most favorable condition for the mechanical and microstructural development of RMC concrete samples. On the whole, the results emerging from this study demonstrated that the determination of optimum CO<sub>2</sub> concentration is dependent on the overall goal. While higher concentrations (20%) are beneficial for rapid early strength gain, lower concentrations (5%) can also deliver the same performance if given sufficient time. Nevertheless, the high contents of unreacted (i.e. via hydration and carbonation) binder revealed in this study clearly indicate the great potential of RMC in providing even better performance than those reported.

## **Acknowledgement**

N.T. Dung and C. Unluer received funding from the Singapore-MIT Alliance for Research and Technology Innovation Centre (ING1510112-ENG). R. Hay and K. Celik are grateful to Dr. Abdullah Khalil and Core Technology Platform (CTP) experts, specifically Dr. James Weston and Dr. Liang Li, of New York University Abu Dhabi (NYUAD) for their help during the experiments. This work was supported by the NYUAD Center for Interacting Urban Networks (CITIES), funded by Tamkeen under the NYUAD Research Institute Award CG001 and by the Swiss Re Institute under the Quantum Cities™ initiative.

## References

- [1] M. Liska, A. Al-Tabbaa, Ultra-green construction: reactive magnesia masonry products, *Waste and Resource Management*, 162, (2008) 185-196.
- [2] C. Sonat, C.H. Lim, M. Liska, C. Unluer, Recycling and reuse of reactive MgO cements—A feasibility study, *Construction and Building Materials*, 157, (2017) 172-181.
- [3] G. Ellis, Are There Any Practical Alternatives to the Manufacture of Portland Cement Clinker?, *Journal of The Chinese Ceramic Society*, 40, (2012) 61-68.
- [4] E. Gartner, T. Sui, Alternative cement clinkers, *Cement and Concrete Research*, 114, (2018) 27-39.
- [5] J.J. Thomas, S. Musso, I. Prestini, Kinetics and activation energy of magnesium oxide hydration, *Journal of the American Ceramic Society*, 97, (2014) 275-282.
- [6] N.T. Dung, C. Unluer, Performance of reactive MgO concrete under increased CO<sub>2</sub> dissolution, *Cement and Concrete Research*, 118, (2019) 92-101.
- [7] R. Hay, K. Celik, Accelerated carbonation of reactive magnesium oxide cement (RMC)-based composite with supercritical carbon dioxide (scCO<sub>2</sub>), *Journal of Cleaner Production*, 248, (2020) 119282.
- [8] F. Winnefeld, E. Epifania, F. Montagnaro, E.M. Gartner, Further studies of the hydration of MgO-hydromagnesite blends, *Cement and Concrete Research*, 126, (2019) 105912.
- [9] V.-T. Luong, R. Amal, J.A. Scott, S. Ehrenberger, T. Tran, A comparison of carbon footprints of magnesium oxide and magnesium hydroxide produced from conventional processes, *Journal of Cleaner Production*, 202, (2018) 1035-1044.
- [10] H. Dong, C. Unluer, E.-H. Yang, A. Al-Tabbaa, Recovery of reactive MgO from reject brine via the addition of NaOH, *Desalination*, 429, (2018) 88-95.
- [11] H. Dong, C. Unluer, E.-H. Yang, A. Al-Tabbaa, Synthesis of reactive MgO from reject brine via the addition of NH<sub>4</sub> OH, *Hydrometallurgy*, 169, (2017) 165-172.
- [12] F. Jin, K. Gu, A. Al-Tabbaa, Strength and hydration properties of reactive MgO-activated ground granulated blastfurnace slag paste, *Cement and Concrete Composites*, 57, (2015) 8-16.
- [13] I.M. Power, G.M. Dipple, P.S. Francis, Assessing the carbon sequestration potential of magnesium oxychloride cement building materials, *Cement and Concrete Composites*, 78, (2017) 97-107.
- [14] G. Gadikota, J. Matter, P. Kelemen, A.-h.A. Park, Chemical and morphological changes during olivine carbonation for CO<sub>2</sub> storage in the presence of NaCl and NaHCO<sub>3</sub>, *Physical Chemistry Chemical Physics*, 16, (2014) 4679-4693.

733 [15] G. Montes-Hernandez, F. Renard, R. Chiriac, N. Findling, F. Toche, Rapid Precipitation  
734 of Magnesite Microcrystals from  $\text{Mg}(\text{OH})_2\text{-H}_2\text{O-CO}_2$  Slurry Enhanced by NaOH and a Heat-  
735 Aging Step (from  $\sim 20$  to  $90^\circ\text{C}$ ), *Crystal Growth & Design*, 12, (2012) 5233-5240.

736 [16] K.J. Fricker, A.-H.A. Park, Effect of  $\text{H}_2\text{O}$  on  $\text{Mg}(\text{OH})_2$  carbonation pathways for  
737 combined  $\text{CO}_2$  capture and storage, *Chemical Engineering Science*, 100, (2013) 332-341.

738 [17] J. Fagerlund, J. Highfield, R. Zevenhoven, Kinetics studies on wet and dry gas–solid  
739 carbonation of  $\text{MgO}$  and  $\text{Mg}(\text{OH})_2$  for  $\text{CO}_2$  sequestration, *RSC Advances*, 2, (2012) 10380-  
740 10393.

741 [18] A.L. Harrison, I.M. Power, G.M. Dipple, Accelerated Carbonation of Brucite in Mine  
742 Tailings for Carbon Sequestration, *Environmental Science & Technology*, 47, (2013) 126-134.

743 [19] L.J. Vandeperre, A. Al-Tabbaa, Accelerated carbonation of reactive  $\text{MgO}$  cements,  
744 *Advances in Cement Research*, 19, (2007) 67-79.

745 [20] N.T. Dung, C. Unluer, Development of  $\text{MgO}$  concrete with enhanced hydration and  
746 carbonation mechanisms, *Cement and Concrete Research*, 103, (2018) 160-169.

747 [21] R. Zhang, D.K. Panesar, Water absorption of carbonated reactive  $\text{MgO}$  concrete and its  
748 correlation with the pore structure, *Journal of  $\text{CO}_2$  Utilization*, 24, (2018) 350-360.

749 [22] N.T. Dung, A. Lesimple, R. Hay, K. Celik, C. Unluer, Formation of carbonate phases and  
750 their effect on the performance of reactive  $\text{MgO}$  cement formulations, *Cement and Concrete*  
751 *Research*, 125, (2019) 105894.

752 [23] J.T. Klopogge, W.N. Martens, L. Nothdurft, L.V. Duong, G.E. Webb, Low temperature  
753 synthesis and characterization of nesquehonite, *Journal of Materials Science Letters*, 22, (2003)  
754 825-829.

755 [24] G.W. Beall, E.-S.M. Duraia, F. El-Tantawy, F. Al-Hazmi, A.A. Al-Ghamdi, Rapid  
756 fabrication of nanostructured magnesium hydroxide and hydromagnesite via microwave-  
757 assisted technique, *Powder Technology*, 234, (2013) 26-31.

758 [25] V. Ferrini, C. De Vito, S. Mignardi, Synthesis of nesquehonite by reaction of gaseous  $\text{CO}$   
759  $2$  with  $\text{Mg}$  chloride solution: its potential role in the sequestration of carbon dioxide, *Journal*  
760 *of hazardous materials*, 168, (2009) 832-837.

761 [26] N.T. Dung, C. Unluer, Sequestration of  $\text{CO}_2$  in reactive  $\text{MgO}$  cement-based mixes with  
762 enhanced hydration mechanisms, *Construction and Building Materials*, 143, (2017) 71-82.

763 [27] N.T. Dung, C. Unluer, Improving the Carbonation of Reactive  $\text{MgO}$  Cement Concrete via  
764 the Use of  $\text{NaHCO}_3$  and  $\text{NaCl}$ , *Journal of Materials in Civil Engineering*, 30, (2018).



765 [28] L. Mo, D.K. Panesar, Accelerated carbonation—A potential approach to sequester CO<sub>2</sub> in  
 766 cement paste containing slag and reactive MgO, *Cement and Concrete Composites*, 43, (2013)  
 767 69-77.

768 [29] N.T. Dung, C. Unluer, Carbonated MgO concrete with improved performance: The  
 769 influence of temperature and hydration agent on hydration, carbonation and strength gain,  
 770 *Cement and Concrete Composites*, 82, (2017) 152-164.

771 [30] P. De Silva, L. Bucea, D.R. Moorehead, V. Sirivivatnanon, Carbonate binders: Reaction  
 772 kinetics, strength and microstructure, *Cement and Concrete Composites*, 28, (2006) 613-620.

773 [31] C. Unluer, A. Al-Tabbaa, Enhancing the carbonation of MgO cement porous blocks  
 774 through improved curing conditions, *Cement and Concrete Research*, 59, (2014) 55-65.

775 [32] M. Nedeljković, B. Ghiassi, S. van der Laan, Z. Li, G. Ye, Effect of curing conditions on  
 776 the pore solution and carbonation resistance of alkali-activated fly ash and slag pastes, *Cement*  
 777 *and Concrete Research*, 116, (2019) 146-158.

778 [33] G. Constantinides, F.-J. Ulm, The nanogranular nature of C–S–H, *Journal of the*  
 779 *Mechanics and Physics of Solids*, 55, (2007) 64-90.

780 [34] P. Trtik, B. Münch, P. Lura, A critical examination of statistical nanoindentation on model  
 781 materials and hardened cement pastes based on virtual experiments, *Cement and Concrete*  
 782 *Composites*, 31, (2009) 705-714.

783 [35] A. Technologies, Nano Indenter G200, Palo Alto, CA 94304 USA, 2013.

784 [36] C.-S. Zha, H.-k. Mao, R.J. Hemley, Elasticity of MgO and a primary pressure scale to 55  
 785 GPa, *Proceedings of the National Academy of Sciences*, 97, (2000) 13494-13499.

786 [37] M. de Jong, W. Chen, T. Angsten, A. Jain, R. Notestine, A. Gamst, M. Sluiter, C. Krishna  
 787 Ande, S. van der Zwaag, J.J. Plata, C. Toher, S. Curtarolo, G. Ceder, K.A. Persson, M. Asta,  
 788 Charting the complete elastic properties of inorganic crystalline compounds, *Scientific Data*,  
 789 2, (2015) 150009.

790 [38] M. Liska, L.J. Vandeperre, A. Al-Tabbaa, Influence of carbonation on the properties of  
 791 reactive magnesia cement-based pressed masonry units, *Advances in cement research*, 20,  
 792 (2008) 53-64.

793 [39] O. Kangal, C. Firat, A. Güney, Flotation properties of unusual carbonates: huntite and  
 794 hydromagnesite, *Minerals Engineering*, 18, (2005) 631-634.

795 [40] E.E. Coleyshaw, G. Crump, W.P. Griffith, Vibrational spectra of the hydrated carbonate  
 796 minerals ikaite, monohydrocalcite, lansfordite and nesquehonite, *Spectrochimica Acta Part A:*  
 797 *Molecular and Biomolecular Spectroscopy*, 59, (2003) 2231-2239.

798 [41] A.V. Saetta, B.A. Schrefler, R.V. Vitaliani, 2 — D model for carbonation and  
799 moisture/heat flow in porous materials, *Cement and Concrete Research*, 25, (1995) 1703-1712.

800 [42] W. Cheng, Z. Li, Nucleation kinetics of nesquehonite ( $\text{MgCO}_3 \cdot 3\text{H}_2\text{O}$ ) in the  
801  $\text{MgCl}_2$ – $\text{Na}_2\text{CO}_3$  system, *Journal of Crystal Growth*, 312, (2010) 1563-1571.

802 [43] J. Chen, Y. Song, D. Shan, E.-H. Han, Study of the in situ growth mechanism of Mg–Al  
803 hydrotalcite conversion film on AZ31 magnesium alloy, *Corrosion Science*, 63, (2012) 148-  
804 158.

805 [44] V. Vágvölgyi, R.L. Frost, M. Hales, A. Locke, J. Kristóf, E. Horváth, Controlled rate  
806 thermal analysis of hydromagnesite, *Journal of Thermal Analysis and Calorimetry*, 92, (2008)  
807 893-897.

808 [45] R.L. Frost, S.J. Palmer, Infrared and infrared emission spectroscopy of nesquehonite  
809  $\text{Mg}(\text{OH})(\text{HCO}_3) \cdot 2\text{H}_2\text{O}$ —implications for the formula of nesquehonite, *Spectrochimica Acta*  
810 Part A: Molecular and Biomolecular Spectroscopy, 78, (2011) 1255-1260.

811 [46] R.L. Frost, S. Bahfenne, J. Graham, Raman spectroscopic study of the magnesium-  
812 carbonate minerals—artinite and dypingite, *Journal of Raman Spectroscopy: An International*  
813 *Journal for Original Work in all Aspects of Raman Spectroscopy, Including Higher Order*  
814 *Processes, and also Brillouin and Rayleigh Scattering*, 40, (2009) 855-860.

815 [47] H. Ren, Z. Chen, Y. Wu, M. Yang, J. Chen, H. Hu, J. Liu, Thermal characterization and  
816 kinetic analysis of nesquehonite, hydromagnesite, and brucite, using TG–DTG and DSC  
817 techniques, *Journal of Thermal Analysis and Calorimetry*, 115, (2014) 1949-1960.

818 [48] J. Lanas, J.I. Alvarez, Dolomitic lime: thermal decomposition of nesquehonite,  
819 *Thermochimica Acta*, 421, (2004) 123-132.

820 [49] Y. Sawada, J. Yamaguchi, O. Sakurai, K. Uematsu, N. Mizutani, M. Kato, Thermal  
821 decomposition of basic magnesium carbonates under high-pressure gas atmospheres,  
822 *Thermochimica Acta*, 32, (1979) 277-291.

823 [50] Y. Sawada, K. Uematsu, N. Mizutani, M. Kato, Thermal decomposition of  
824 hydromagnesite  $4\text{MgCO}_3 - \text{Mg}(\text{OH})_2 - 4\text{H}_2\text{O}$  under different partial pressures of carbon  
825 dioxide, *Thermochimica Acta*, 27, (1978) 45-59.

826 [51] D. Winslow, D. Liu, The pore structure of paste in concrete, *Cement and Concrete*  
827 *Research*, 20, (1990) 227-235.

828 [52] S. Chinchón-Payá, C. Andrade, S. Chinchón, Indicator of carbonation front in concrete as  
829 substitute to phenolphthalein, *Cement and Concrete Research*, 82, (2016) 87-91.

830 [53] S. Teir, S. Eloneva, C.-J. Fogelholm, R. Zevenhoven, Stability of calcium carbonate and  
831 magnesium carbonate in rainwater and nitric acid solutions, *Energy Conversion and*  
832 *Management*, 47, (2006) 3059-3068.

833 [54] R.L. Frost, S. Bahfenne, J. Graham, W.N. Martens, Thermal stability of artinite, dypingite  
834 and brugnatellite—Implications for the geosequestration of green house gases, *Thermochimica*  
835 *Acta*, 475, (2008) 39-43.

836 [55] C. Kuenzel, F. Zhang, V. Ferrándiz-Mas, C.R. Cheeseman, E.M. Gartner, The mechanism  
837 of hydration of MgO-hydromagnesite blends, *Cement and Concrete Research*, 103, (2018) 123-  
838 129.

839

## List of Tables

Table 1 Chemical composition and physical properties of RMC.

	Chemical composition (%)							Physical properties	
	MgO	SiO <sub>2</sub>	CaO	R <sub>2</sub> O <sub>3</sub>	K <sub>2</sub> O	Na <sub>2</sub> O	LOI	Specific gravity (g/cm <sup>3</sup> )	Specific surface area (m <sup>2</sup> /g)
RMC	>91.5	2.0	1.6	1.0	-	-	4.0	3.0	16.3

Table 2 Content of different phases within RMC samples cured under different CO<sub>2</sub> concentrations for 7 days.

	Content (wt.%)			
	Amb	C5	C10	C20 [22]
Periclase	16.8	19.7	27.4	34.9
Brucite	77.3	69.0	61.5	51.5
Artinite	4.4	5.1	6.9	5.3
Hydromagnesite	0.5	1.9	0.1	4.2
Nesquehonite	1.0	4.2	4.1	4.1

Table 3 Mass loss of all RMC samples cured under different CO<sub>2</sub> concentrations for 7 and 28 days, measured by TG-DTG.

Samples		Mass loss (wt.%)			
		Dehydration	Dehydroxylation	Decarbonation	Total
7 days	Amb	2.0	21.3	3.3	26.6
	C5	6.5	23.4	5.0	34.9
	C10	7.7	22.1	5.6	35.5
	C20 [22]	9.1	21.9	6.1	37.1
28 days	Amb	2.6	22.1	4.9	29.6
	C5	11.4	25.5	6.2	43.1
	C10	9.1	24.2	6.8	40.1
	C20 [22]	9.5	22.7	6.6	38.7

## List of Figures

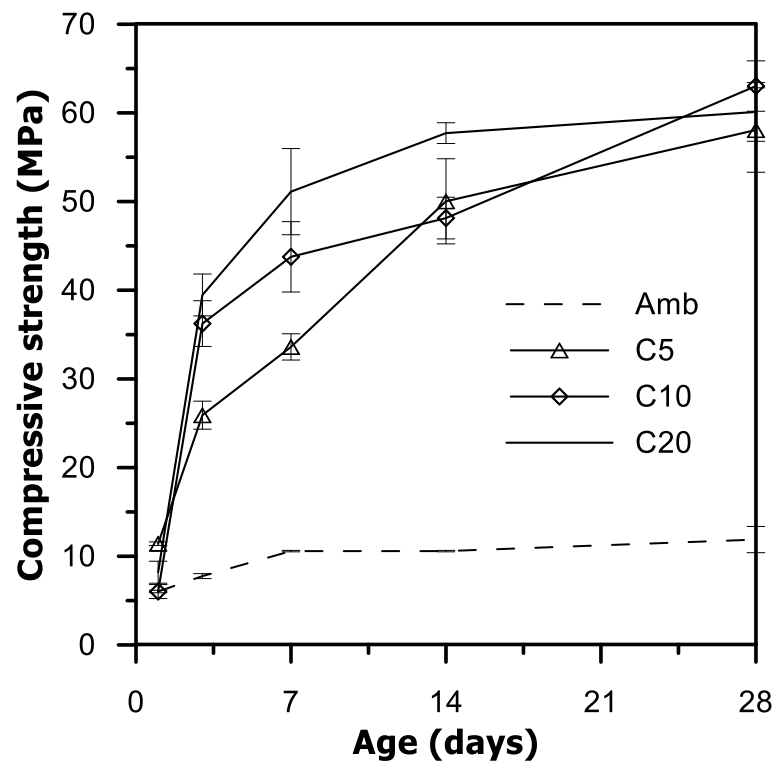


Fig. 1 Compressive strength of RMC concrete subjected to different CO<sub>2</sub> concentrations

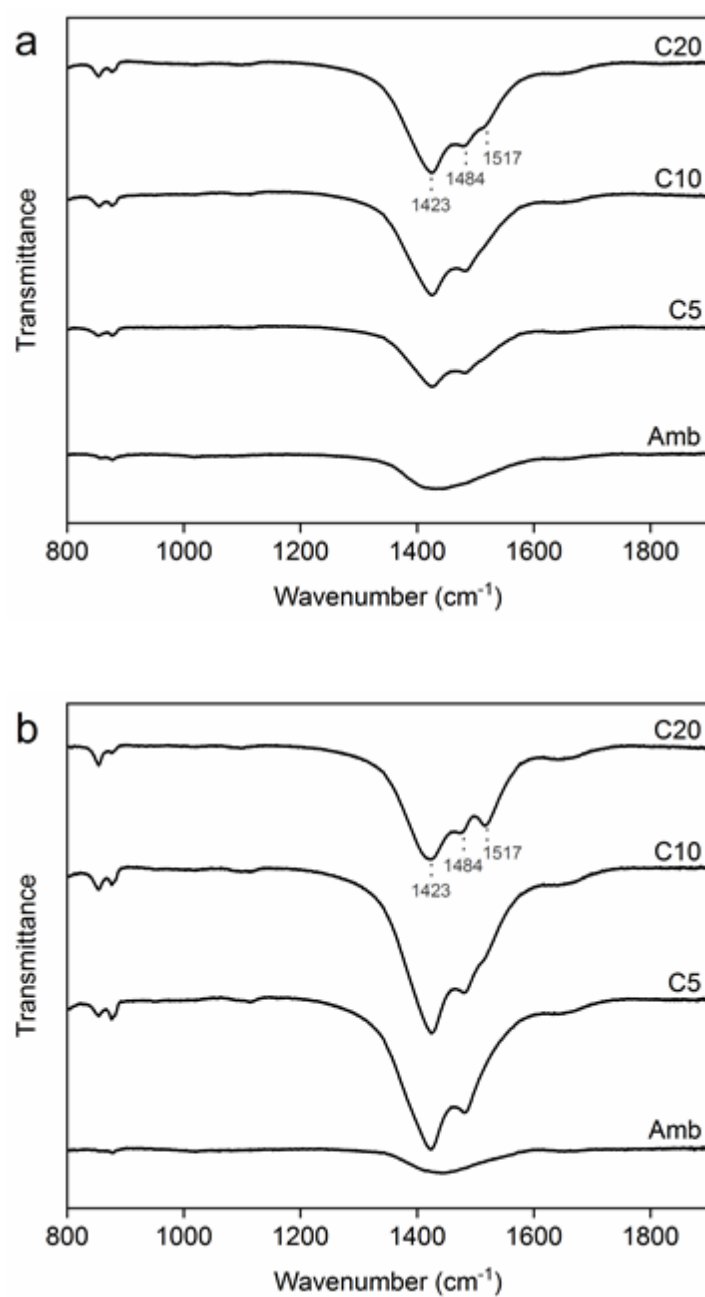


Fig. 2 FTIR spectra of RMC samples cured under different CO<sub>2</sub> concentrations for (a) 7 and (b) 28 days



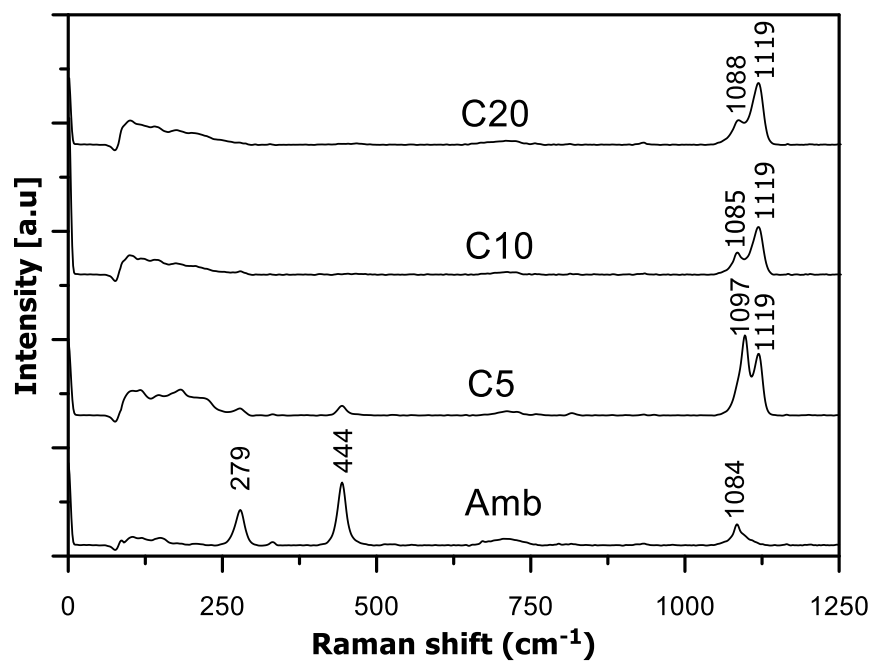


Fig. 3 Raman spectra of RMC samples cured under different CO<sub>2</sub> concentrations for 7 days

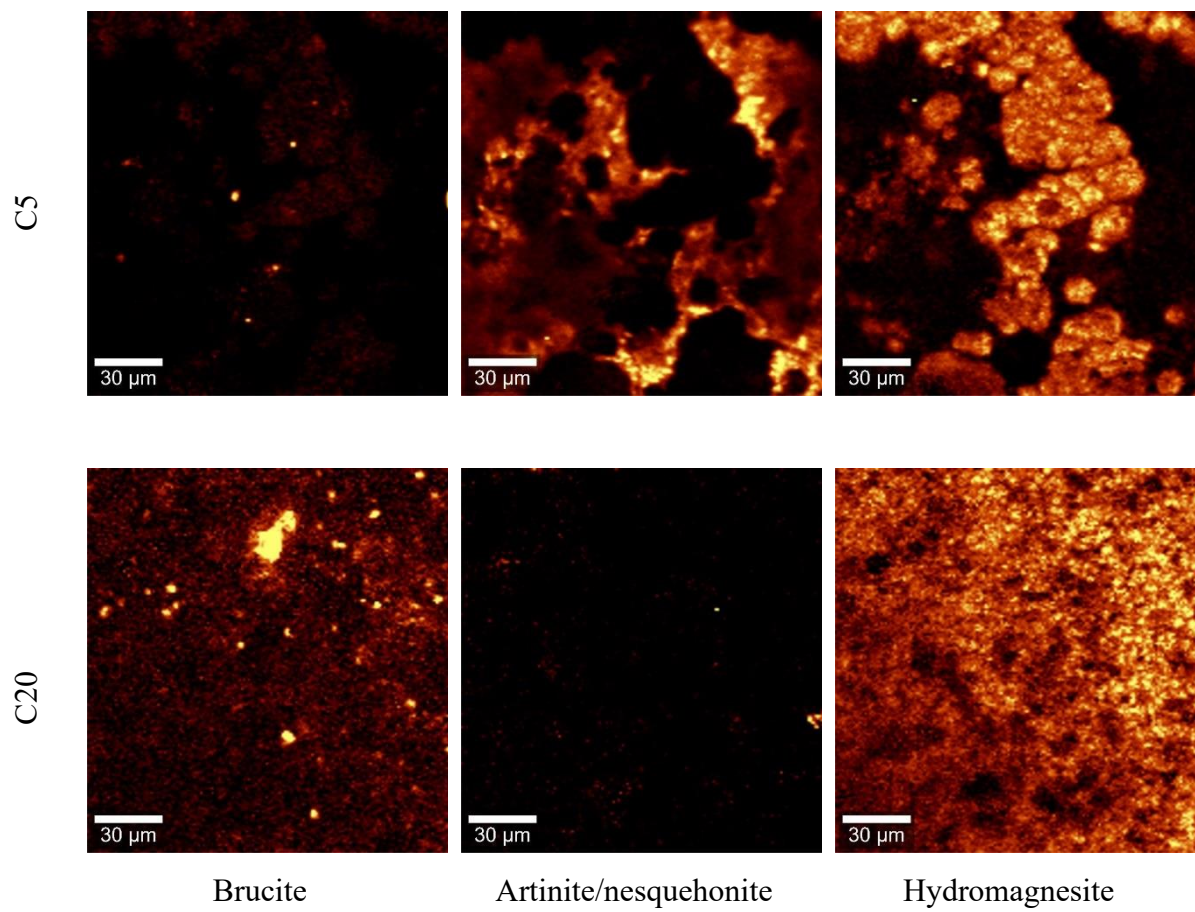


Fig. 4 Phase distributions within C5 and C20 samples after 7 days of carbonation

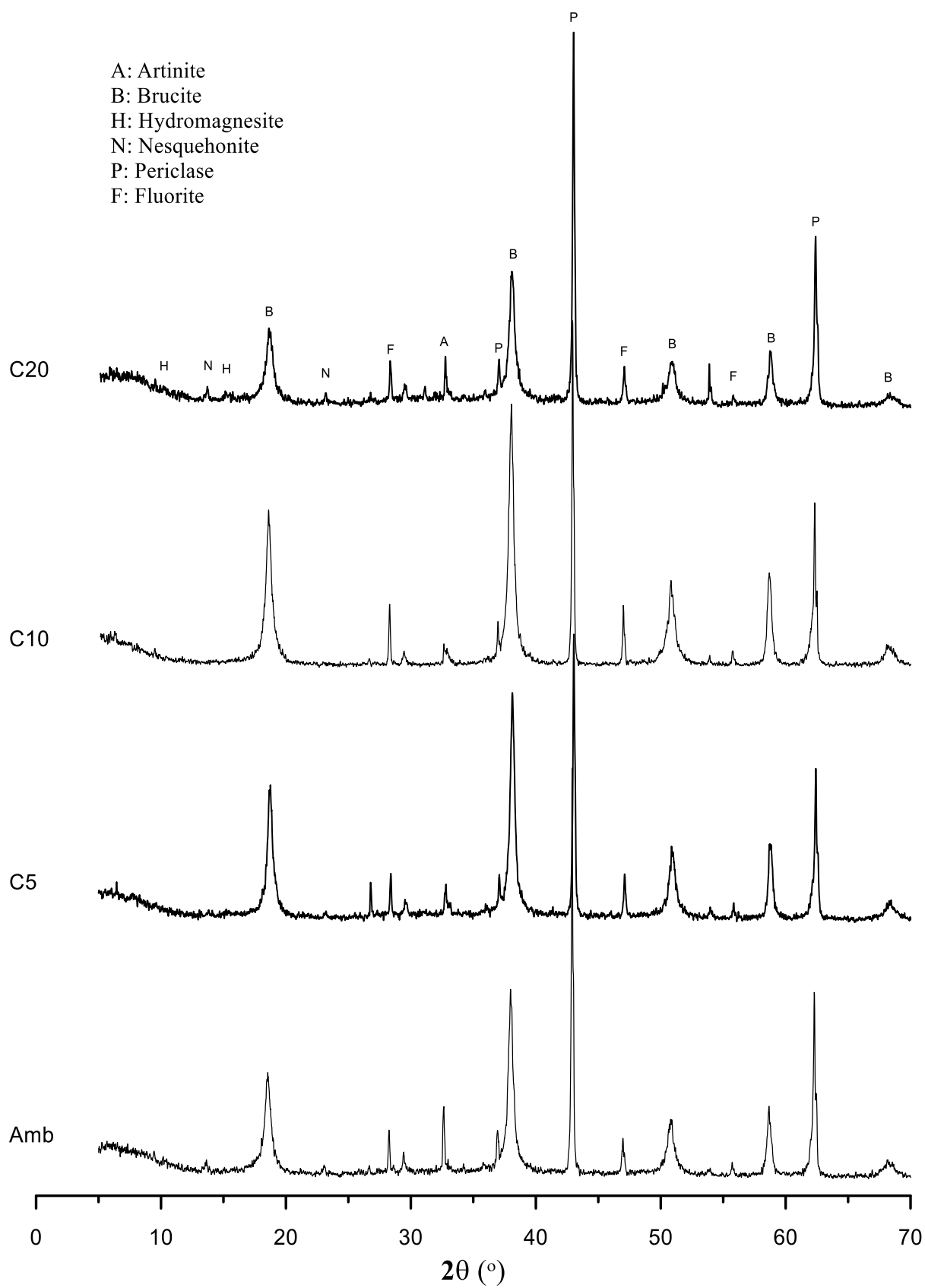


Fig. 5 XRD patterns of RMC samples cured under different CO<sub>2</sub> concentrations for 7 days

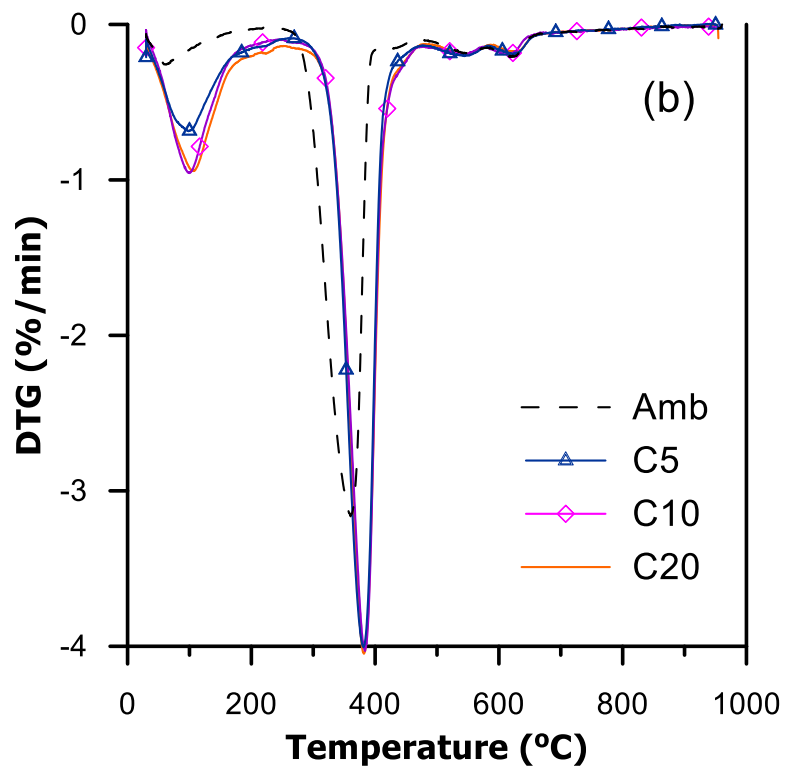
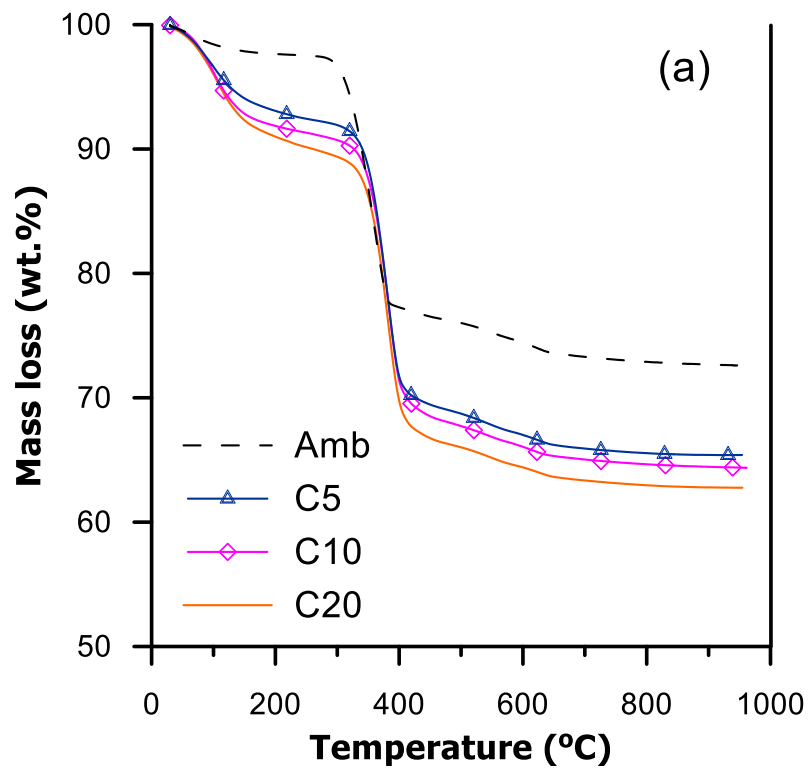


Fig. 6 TGA results of RMC samples cured under different CO<sub>2</sub> concentrations for 7 days: (a) TG and (b) DTG

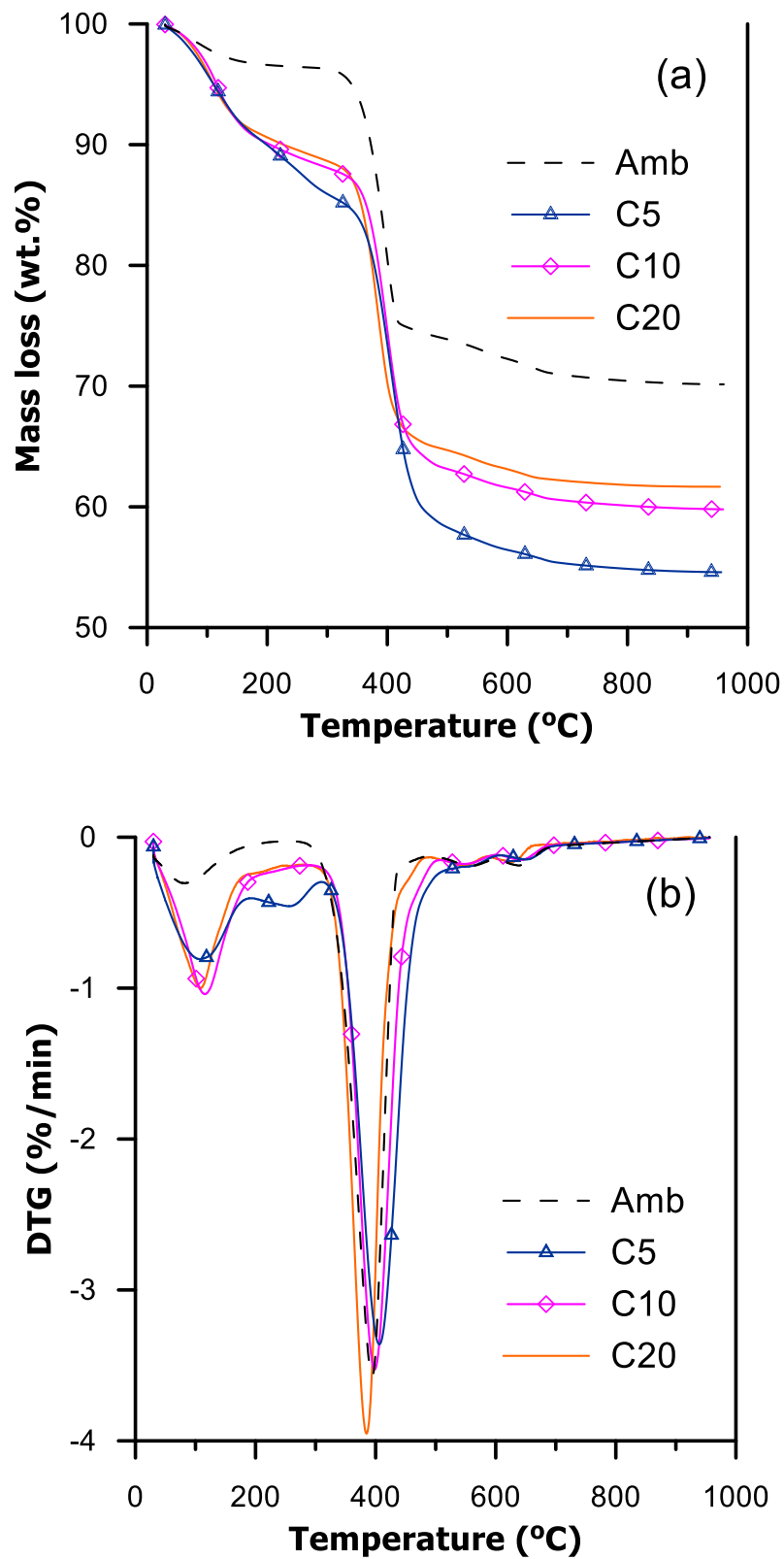
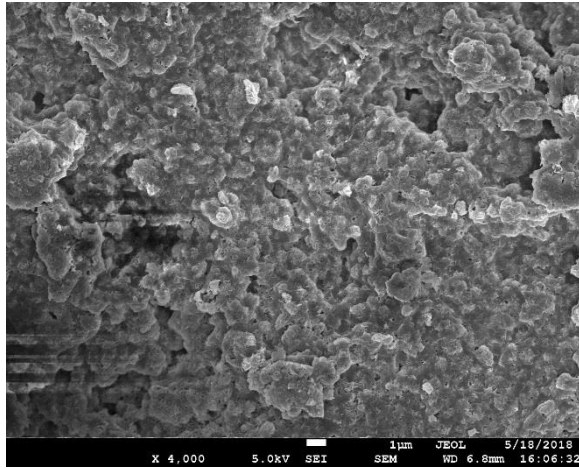
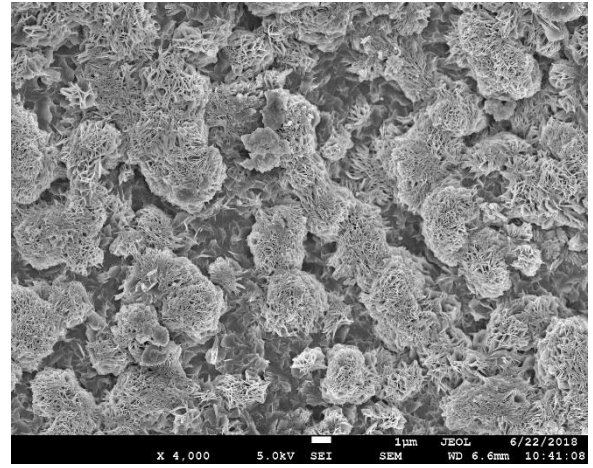


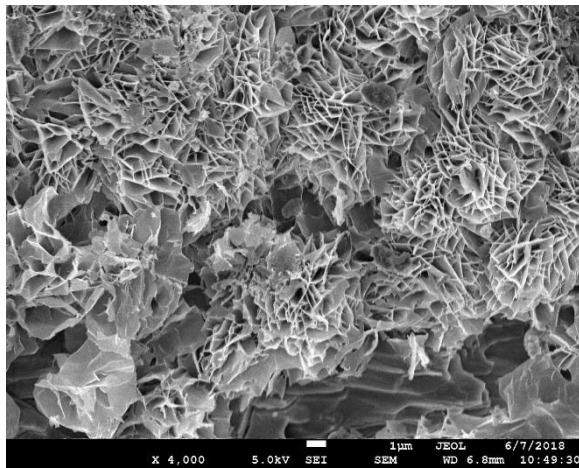
Fig. 7 TGA results of RMC samples cured under different CO<sub>2</sub> concentrations for 28 days:  
(a) TG and (b) DTG



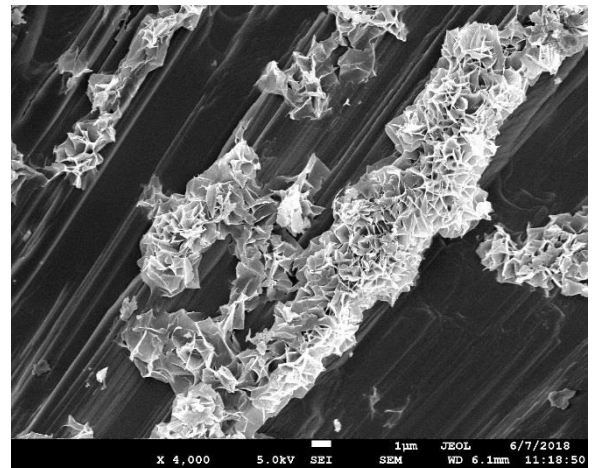
(a)



(b)



(c)



(d)

Fig. 8 SEM images of (a) Amb, (b) C5, (c) C10 and (d) C20 samples after 7 days of curing

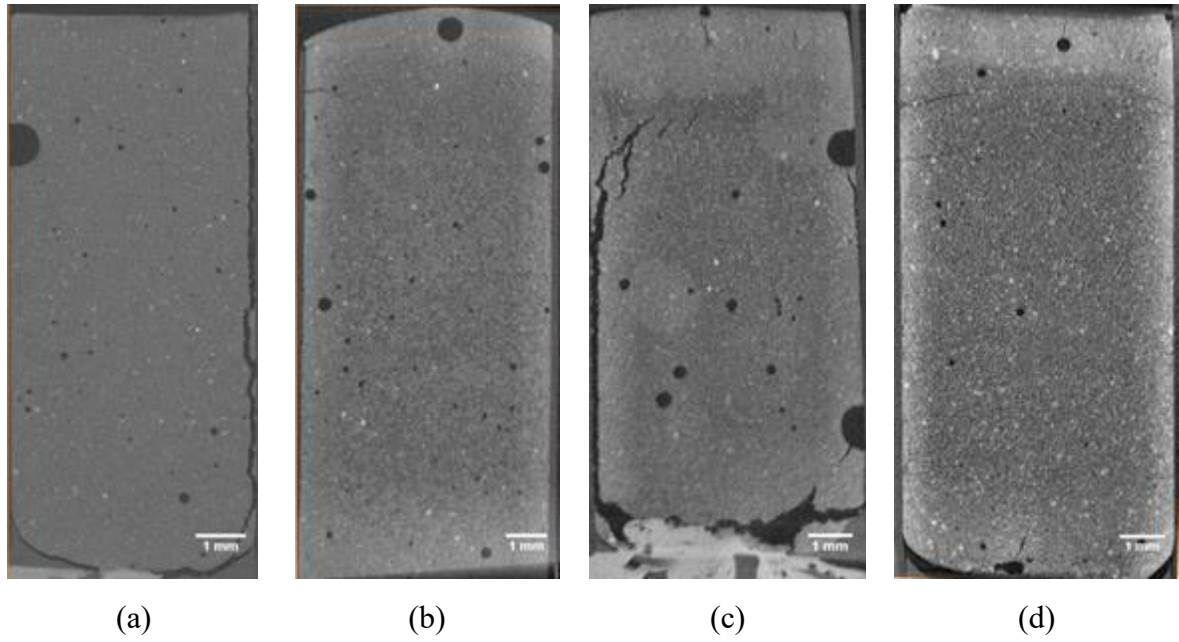


Fig. 9 Vertical cross sections from x-ray micro CT reconstruction of (a) Amb, (b) C5, (c) C10 and (d) C20 samples after 7 days of curing

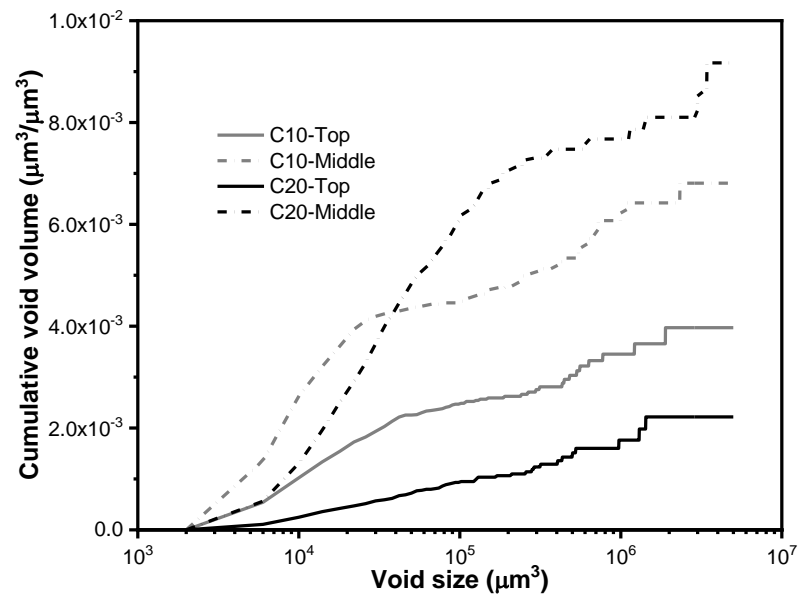


Fig. 10 Cumulative pore volumes within the top and middle regions of C10 and C20 samples after 7 days of carbonation



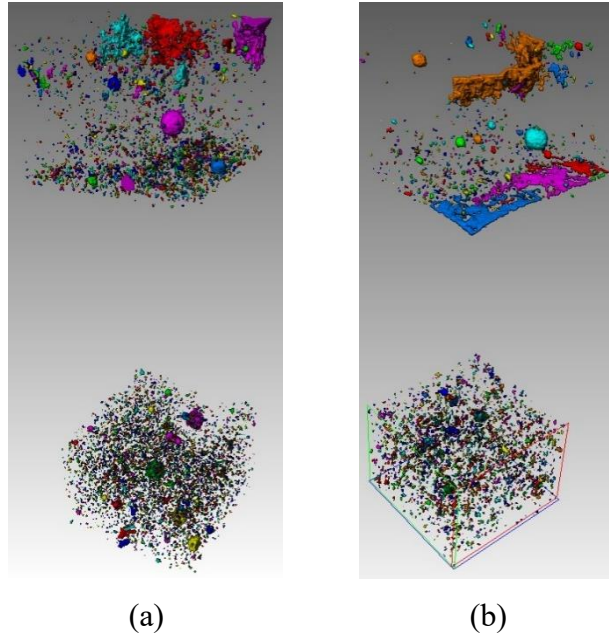


Fig. 11 3D representation of the pore distribution within top and middle ROIs of (a) C10 and (b) C20 samples after 7 days of carbonation

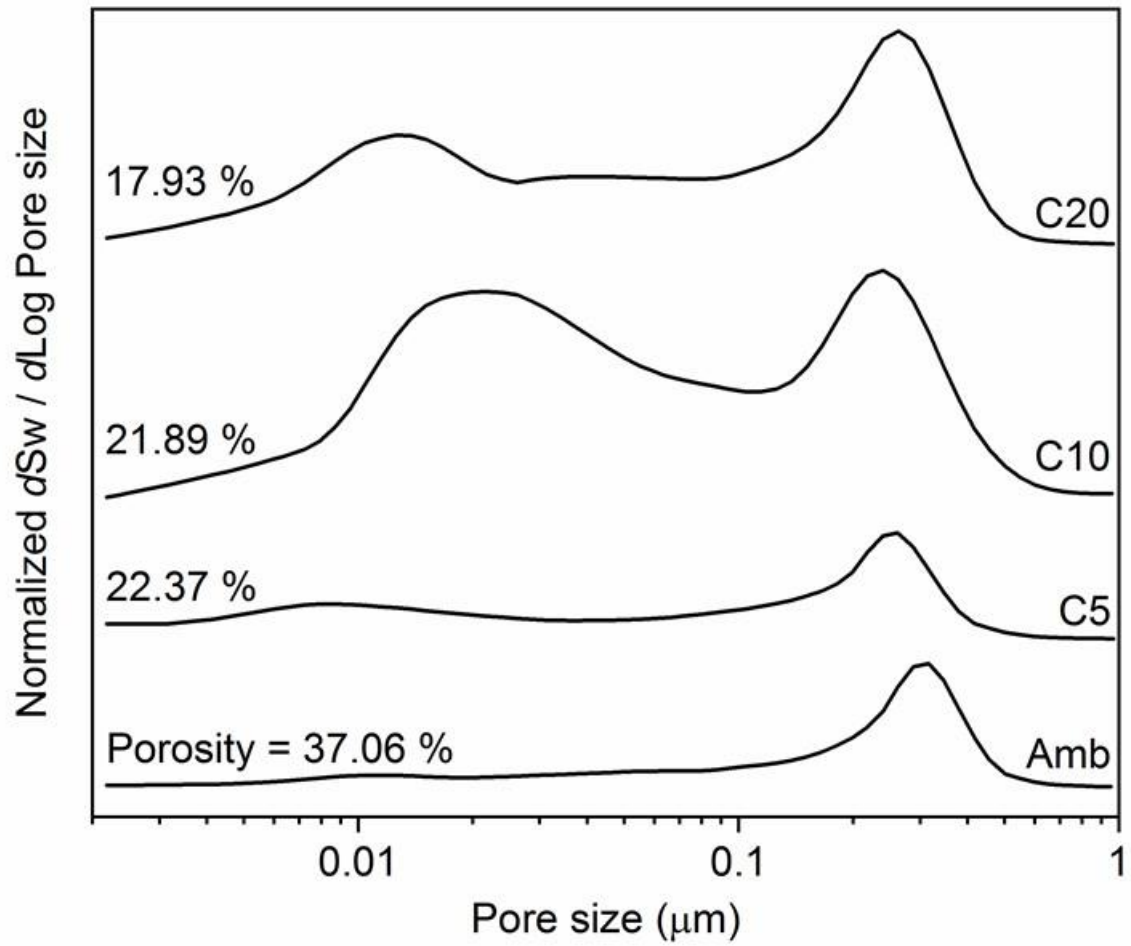


Fig. 12 Average porosity and pore size distribution of RMC samples cured under different  $\text{CO}_2$  concentrations for 7 days

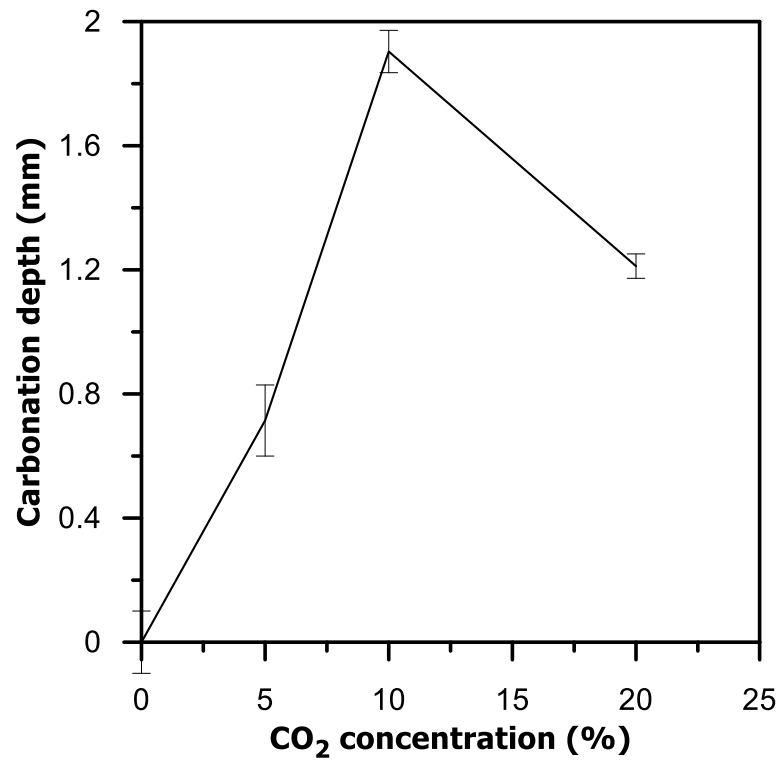


Fig. 13 1-D carbonation depth of RMC pastes cured under different CO<sub>2</sub> concentrations for 7 days

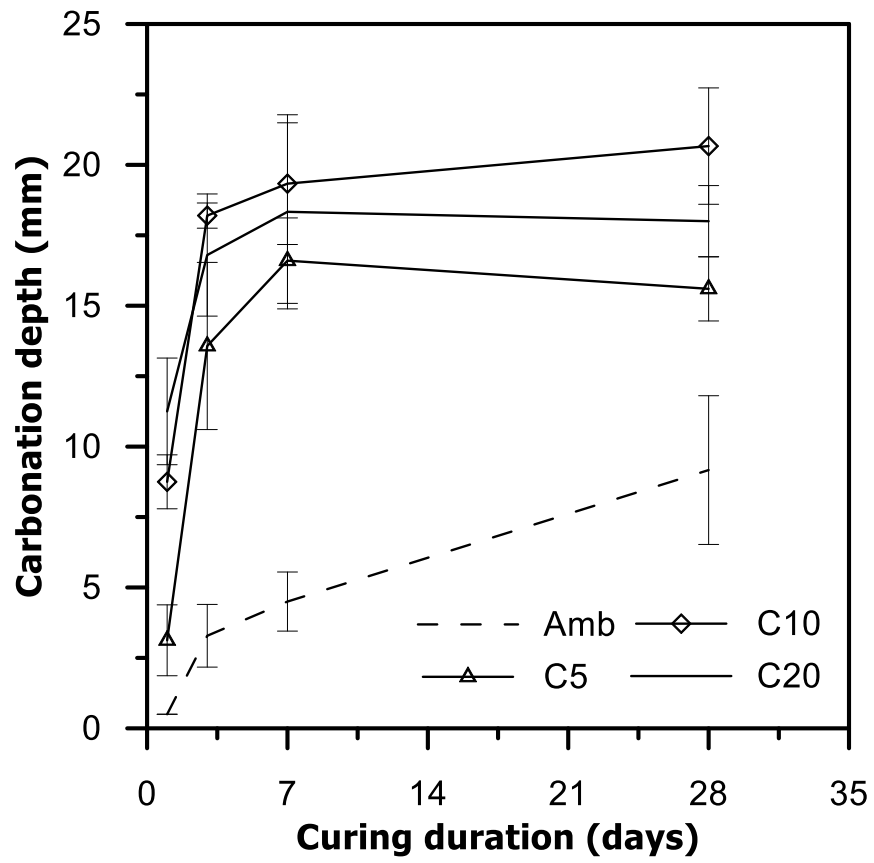


Fig. 14 Carbonation depth of RMC samples cured under different CO<sub>2</sub> concentrations

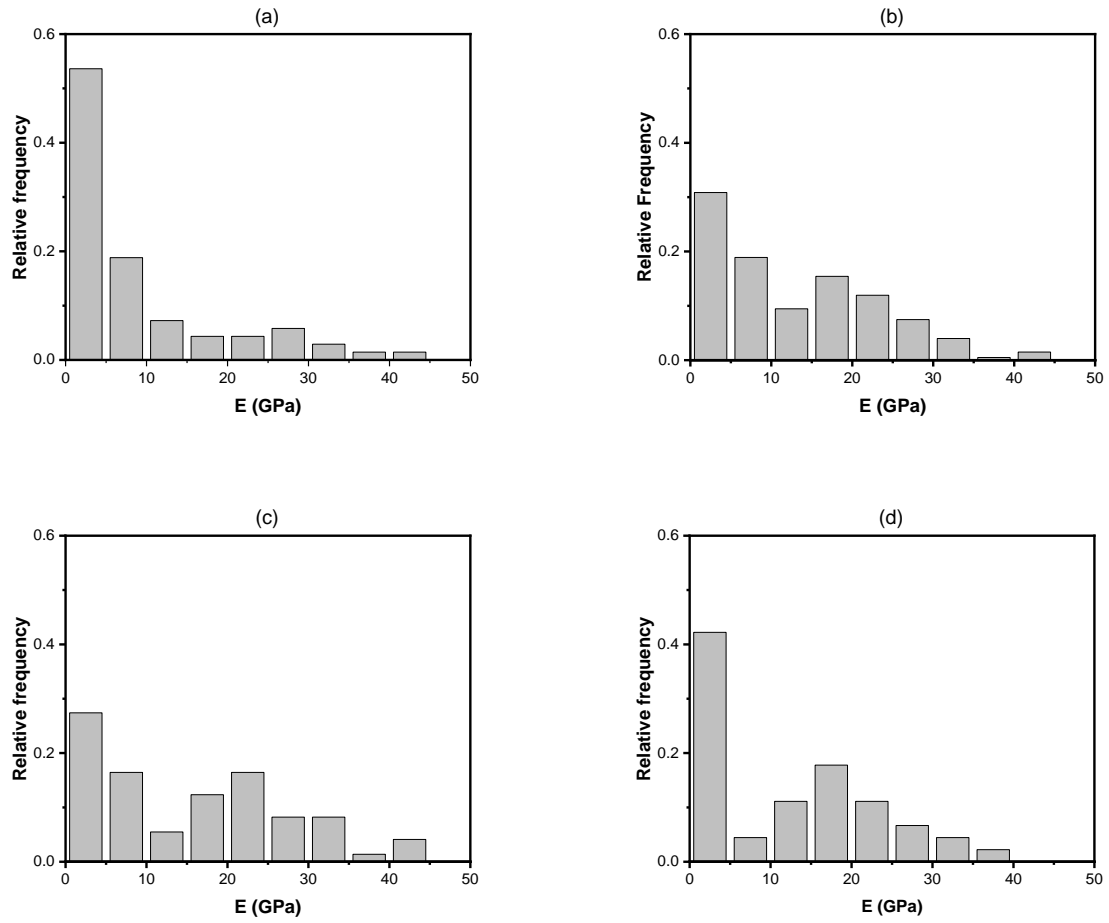


Fig. 15 Nano-indentation results for (a) Amb, (b) C5, (c) C10 and (d) C20 samples after 7 days of curing

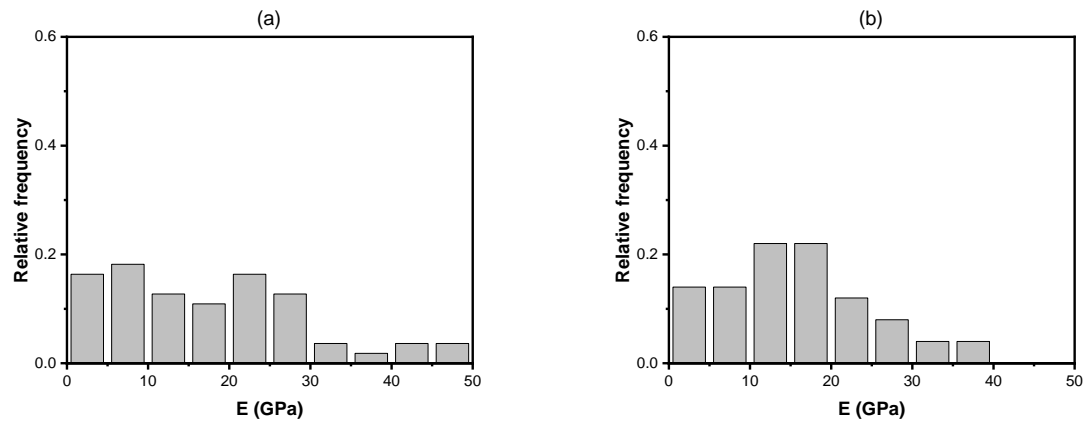


Fig. 16 Nano-indentation results for (a) C10 and (b) C20 samples after 28 days of curing